

# Lattice calculation of thermal properties of low-density neutron matter with pionless $NN$ effective field theory

T. Abe<sup>1</sup> \* and R. Seki<sup>2</sup>

<sup>1</sup> *Department of Physics, Tokyo Institute of Technology, Meguro, Tokyo 152-8551, Japan*

<sup>2</sup> *Department of Physics and Astronomy, California State University,  
Northridge, Northridge, CA 91330, USA*

(Dated: October 25, 2018)

## Abstract

Thermal properties of low-density neutron matter are investigated by determinantal quantum Monte Carlo lattice calculations on 3+1 dimensional cubic lattices. Nuclear effective field theory (EFT) is applied using the pionless single- and two-parameter neutron-neutron interactions, determined from the  $^1S_0$  scattering length and effective range. The determination of the interactions and the calculations of neutron matter are carried out consistently by applying EFT power counting rules. The thermodynamic limit is taken by the method of finite-size scaling, and the continuum limit is examined in the vanishing lattice filling limit. The  $^1S_0$  pairing gap at  $T \approx 0$  is computed directly from the off-diagonal long-range order of the spin pair-pair correlation function and is found to be approximately 30% smaller than BCS calculations with the conventional nucleon-nucleon potentials. The critical temperature  $T_c$  of the normal-to-superfluid phase transition and the pairing temperature scale  $T^*$  are determined, and the temperature-density phase diagram is constructed. The physics of low-density neutron matter is clearly identified as being a BCS-Bose-Einstein condensation crossover.

PACS numbers: 21.60.Ka, 21.65.-f, 26.60.-c

---

\* Current address: Center for Nuclear Study, Graduate School of Science, the University of Tokyo, RIKEN campus, Wako, Saitama 351-0198, Japan.

## I. INTRODUCTION

Neutron matter is of great interest in nuclear physics as a quantum many-body system. The  $^1S_0$  nucleon-nucleon ( $NN$ ) interaction is strongly attractive, dominating the physics of neutron matter. The interaction yields the negative (in our convention) scattering length  $a_0$  of an unnaturally large magnitude ( $\approx 20$  fm), with the effective range  $r_0$  of a moderate (natural) size of about twice the pion wavelength ( $\approx 2.8$  fm). The value of  $a_0$  implies that the strongly attractive interaction nearly forms a bound state. By this pairing, neutron matter is a strongly interacting many-body system, which must be treated nonperturbatively [1].

The strong neutron pairing generates a pairing gap that creates superfluidity in neutron matter. Superfluidity in neutron matter is of astronomical interest because of the close relation to the internal structure and thermal evolution of neutron stars [2, 3].  $^1S_0$  and  $^3P_2$ - $^3F_2$  superfluidity are believed to be realized in the inner crust and in the core region of neutron stars, respectively, and to contribute to the thermodynamic and dynamic properties of the stars.

Neutron pairing is also considered important for understanding the structure of neutron-rich unstable nuclei. Neutron-neutron correlations are expected to be a crucial ingredient in the weakly bound, surface structure near the neutron drip line; and for the surface structure, neutron pairing in neutron matter must be well understood [1, 4, 5, 6].

Investigations over many years have provided much understanding of the physics of thermodynamic properties of neutron matter [7, 8, 9], but reliable quantitative information of the thermal properties has not been fully available [1, 2]. For example, the  $^1S_0$  pairing gap at zero temperature  $\Delta$  had been firmly established *in the BCS approximation*, as evident in the fact that various conventional  $NN$  potentials have provided nearly the same  $\Delta_{\text{BCS}}$  as a function of neutron matter density [10, 11]. Many-body calculations beyond the BCS mean-field approximation, however, have yielded  $\Delta$  of various magnitudes, generally smaller than the BCS values, some even by a factor of 2 or more. Quantum Monte Carlo calculations, based on a nonperturbative approach, have also been used on the  $\Delta$  determination. The Green's function Monte Carlo (GFMC) method, quite successful in treating the ground-state properties of finite nuclei by the use of the conventional  $NN$  potentials [12], has yielded  $\Delta$  in the low-density region ( $k_F \lesssim 0.6 \text{ fm}^{-1}$ ), smaller than  $\Delta_{\text{BCS}}$  [13, 14] but not as small as those obtained by some of the many-body calculations. Another method closely related to

GFMC, the auxiliary field diffusion Monte Carlo (AFDMC) method, which is also applied to finite nuclei [15], has given  $\Delta$  quite close to  $\Delta_{\text{BCS}}$  [16, 17] and significantly larger than the GFMC  $\Delta$ . We present a more detailed comparison of these works, including ours, in Sec. VII B.

In this paper, we report a quantum Monte Carlo calculation of  $\Delta$  and thermal properties of neutron matter using a method different from the GFMC and the AFDMC methods. The difference is that ours is based on the standard finite-temperature, grand canonical formulation, while the GFMC and AFDMC methods are based on essentially zero-temperature formulations, performed for the ground or specific excited states with a pre-fixed neutron number. Our calculation may be viewed, in a sense, as a nonrelativistic hadronic version of lattice QCD calculations, but it involves different aspects such as those associated with the large numbers of fermions on the lattice [18]. We use a Hamiltonian formulation different from the Lagrangian formulation commonly used in the lattice QCD calculations. Our formulation is not new, as it has been applied in condensed matter physics for many years [19, 20] and has been also applied in nuclear physics [21]. This work is an extension of the latter.

We also use a new ingredient, the  $NN$  interaction based on effective field theory (EFT) [22, 23], in place of the conventional  $NN$  potentials. It is desirable to include pions [24] in the EFT interaction as dynamical degrees of freedom, representing chiral symmetry and its breaking. Our objective is twofold: (1) to apply the  $NN$  EFT interaction to the many-nucleon system of neutron matter by properly applying EFT counting rules, and (2) to determine reliably the thermal properties of neutron matter and their key quantities, such as  $\Delta$ . In the first attempt for achieving this objective, we have chosen a pionless  $NN$  EFT potential with two parameters. The major consequence of this choice is that application of our calculation is limited to the low-density region,  $k_F \lesssim 0.6 \text{ fm}^{-1}$ . Even with this potential, our work has become a relatively large-scale computation, especially because we take the thermodynamic limit and examine the continuum limit. Note that field theoretical aspects of the general approach of this work were discussed a few years ago [25].

Because the pairing in neutron matter is strong, neutron matter should be treated as a strongly correlated fermionic system in the state of BCS-Bose-Einstein condensation (BEC) crossover, which has been receiving much attention in recent years [26]. Traditionally the pairing in neutron matter has been discussed in the framework of the BCS approximation

[27], but the pairing is too strong for a BCS treatment. The pairing strength is characterized by  $1/(k_F a_0)$  and corresponds to the BCS limit with  $1/(k_F a_0) \rightarrow -\infty$  and to the BEC limit with  $1/(k_F a_0) \rightarrow +\infty$  [28]. The range of  $1/(k_F a_0)$  in the low-density region investigated in this work is well in the middle of the two limits,  $-0.8 \lesssim 1/(k_F a_0) \lesssim -0.1$ , and the magnitude of  $1/(k_F a_0)$  becomes smaller for a higher density. We elaborate on the issue of crossover in Sec. VII A.

The limit  $1/(k_F a_0) \rightarrow 0$  corresponds to the unitary limit, to which much attention has been paid lately in the fields of atomic and condensed-matter physics. A fermion pair in the unitary limit forms a zero-energy bound state, thereby yielding a scattering length infinitely long, associated with no classical scale and expected to have a universal feature. Our single-parameter EFT description of low-density neutron matter is close to the unitary limit (rather than to the BCS limit), and we will discuss the relation between the two in an accompanying paper [29]. We emphasize, however, that the close similarity of the two is restricted to the low-density region of neutron matter ( $k_F \lesssim 0.3 \text{ fm}^{-1}$ ), because additional EFT parameters and the pionic contributions needed for the description of the denser region introduce new length scales and make the physics more complicated than that of the unitary limit.

The outline of this paper is as follows. After the Introduction of Sec. I, the basic setup of our calculation is described in Sec. II. In Sec. III, we present how we determine the physical quantities of interest in this work, and in Sec. IV, we show how we carry out their numerical calculation by taking the thermodynamic and continuum limits. In Sec. V, we discuss how the single- and two-parameter calculations are matched. The summary results are shown in Sec. VI, and discussions of the key points in this work are given in Sec. VII. A summary of our work is found in Sec. VIII. We include, in Appendix A, a relevant, short discussion on how the two  $NN$  potential parameters are determined by satisfying EFT counting rules; in Appendix B, a comparison of the physical sizes of a neutron (Cooper) pair and the computational lattices; and, in Appendix C, somewhat detailed technical aspects of our Monte Carlo calculation.

## II. BASIC SETUP

### A. $NN$ EFT Hamiltonian

The nuclear EFT Lagrangian is constructed by including all possible terms allowed by symmetries of the underlying theory of QCD [30]. The  $NN$  potential from the EFT Lagrangian is written in the momentum expansion form

$$V(\mathbf{p}', \mathbf{p}) = c_0(\Lambda) + c_2(\Lambda)(\mathbf{p}^2 + \mathbf{p}'^2) + \cdots - 2c_2(\Lambda)\mathbf{p} \cdot \mathbf{p}' + \cdots, \quad (1)$$

where  $\mathbf{p}$  and  $\mathbf{p}'$  are the  $NN$  center-of-mass momenta, and  $\Lambda$  is the regularization scale. The terms not explicitly shown in Eq. (1) include those in which pions are treated as a dynamical degree of freedom [31]. For the momentum below the pion mass scale, we may neglect the explicit dynamics of chiral symmetry and its breaking by truncating Eq. (1) and including in  $c_0$  and  $c_2$  the consequences of the dynamics. In this work, we use this pionless  $S$ -wave  $NN$  potential with the first two terms in Eq. (1). Generally an EFT potential is regarded as an expansion in terms of  $\mathbf{p}/\mathcal{Q}$  and  $\mathbf{p}'/\mathcal{Q}$  with  $\mathcal{Q}$  setting the momentum scale of the expansion. In our pionless potential, we have  $\mathcal{Q} \gtrsim m_\pi$  ( $m_\pi$ , the pion mass). Note that the potential consists of the central and spin-dependent parts, as  $c_c + \sigma \cdot \sigma' c_\sigma$ , with  $\sigma \cdot \sigma' = -3$  for the  $^1S_0$  state (and  $= +1$  for the  $^3S_1$  state, not considered in this work). We also neglect in this work the  $P$ -wave interaction term starting with the  $\mathbf{p} \cdot \mathbf{p}'$  and the relativistic effects appearing in  $\mathcal{O}(p^4/M^4)$  [32].

Regularization is required for the application of Eq. (1). On a cubic lattice, the lattice spacing  $a$  serves as the regularization scale  $\Lambda$ , approximately as

$$\Lambda \sim \frac{\pi}{a}. \quad (2)$$

$\Lambda$  should generally be set large, at least larger than the momentum  $p$ ,

$$\Lambda > p, \quad (3)$$

or better set

$$\Lambda \gtrsim \mathcal{Q}, \quad (4)$$

corresponding to  $a \lesssim 4.5$  fm for  $\mathcal{Q} \sim m_\pi$  [32, 33]. When the two-nucleon interaction is applied to a many-nucleon system of finite density, an additional constraint is imposed on the value of  $a$ , as discussed in Sec. II C.

On the lattice, the Hamiltonian for our potential takes the discretized form [34]

$$\begin{aligned}\hat{H} = & -t \sum_{\langle i,j \rangle \sigma} \hat{c}_{i\sigma}^\dagger \hat{c}_{j\sigma} + 6t \sum_{i\sigma} \hat{c}_{i\sigma}^\dagger \hat{c}_{i\sigma} \\ & + \frac{1}{a^3} \left[ c_0(a) - \frac{6}{a^2} c_2(a) \right] \sum_i \hat{c}_{i\uparrow}^\dagger \hat{c}_{i\downarrow}^\dagger \hat{c}_{i\downarrow} \hat{c}_{i\uparrow} + \frac{1}{2a^5} c_2(a) \sum_{\langle i,j \rangle \sigma \sigma'} \hat{c}_{i\sigma}^\dagger \hat{c}_{i\sigma} \hat{c}_{j\sigma'}^\dagger \hat{c}_{j\sigma'},\end{aligned}\quad (5)$$

where  $t = 1/(2Ma^2)$ , the hopping parameter ( $M$  is the neutron mass), and  $\langle i, j \rangle$  denotes a restriction on the sum to all neighboring pairs.  $\hat{c}_{i\sigma}^\dagger$  and  $\hat{c}_{i\sigma}$  are the creation and annihilation operators of the neutron, with  $\sigma = \uparrow, \downarrow$ , respectively, at the  $i$ th site.

The neutron-neutron interaction parameters,  $c_0(a)$  and  $c_2(a)$ , are determined from the neutron-neutron scattering phase shift, using the  $^1S_0$  effective range expansion (ERE),

$$p \cot \delta_0(p) = -\frac{1}{a_0} + \frac{1}{2} r_0 p^2 - P r_0^3 p^4 + \mathcal{O}(p^6), \quad (6)$$

where  $P$  is the shape parameter. By dividing both sides by  $\mathcal{Q}$ , we find Eq. (6) is an expansion in terms of the dimensionless quantity  $p^2/\mathcal{Q}^2$ . For  $\mathcal{Q} \approx m_\pi$ , the coefficients of the expansion  $r_0\mathcal{Q}/2$  and  $P(r_0\mathcal{Q})^3$  are of the natural size  $\mathcal{O}(1)$ , while the first coefficient is unnaturally small,  $|1/a_0\mathcal{Q}| \ll 1$ . Phenomenologically the sum of the first two terms in Eq. (6) agrees well with the phase shift up to the center-of-mass momentum of nearly the pion mass  $m_\pi \approx 0.7 \text{ fm}^{-1}$ , or about 40 MeV of the laboratory kinetic energy [35] (see also Ref. [36]). This assures us that  $c_0(a)$  and  $c_2(a)$  are safely determined from  $a_0$  and  $r_0$  for a chosen value of  $a$  [37].

These interaction parameters are determined by consistently applying EFT power counting rules in a way different from a mere phenomenological fitting, as briefly discussed in Appendix A. Because this determination is one of the crucial steps in this work, let us note its key point here:  *$c_2(a)$  and the contributions of the same order must be treated perturbatively* by neglecting the  $\mathcal{O}([c_2(a)]^2)$  contributions, so that  $\mathcal{O}(p^4/\mathcal{Q}^4)$  contributions are consistently neglected. Furthermore, *to be consistent,  $c_2(a)$  and the contributions of the same order must also be treated perturbatively in the neutron matter calculations.* In the next subsection, we discuss how this treatment is formulated for the neutron matter calculation.

In this work, we carry out the neutron matter calculation using Eq. (5) in two different ways: the leading-order (LO) calculation, in which the  $c_2(a)$  contribution and the contributions of the same order are neglected, and the next-to-leading-order (NLO) calculation, in which they are included. The LO and NLO calculations are expected to yield somewhat

different physics, because Eq. (5) is the Hamiltonian of the attractive Hubbard model for the LO calculation, and it is the Hamiltonian of an extended attractive Hubbard model for the NLO calculation [34]. With the neglect of  $\mathcal{O}(p^2/\mathcal{Q}^2)$ , the LO calculation involves the neutrons of low momenta and should be applicable to a low-density region of neutron matter without the perturbative treatment.

An important issue in this work is the density at which the LO and NLO results should be matched. The ERE of Eq. (6) suggests that the center-of-mass momentum of an interacting neutron pair is less than  $\sqrt{2/(|a_0|r_0)} \approx 0.20 \text{ fm}^{-1}$  at the matching density. As a rough estimate, it may be feasible to identify the Fermi momentum  $k_F$  as this momentum and to estimate the density from it [1], but for a rigorous matching, the LO and NLO neutron matter calculations should be carried out for some common densities and their results compared. As it is desirable to avoid excess computer time, we use in this work the following procedure: we carry out the LO and NLO calculations at the common density of  $k_F = 0.3041 \text{ fm}^{-1}$ , where we expect the two results will certainly differ, and then perform similar calculations by lowering the density so as to identify the density that yields the same LO and NLO results (within the statistical uncertainties). The matching using this procedure is elaborated in Sec. V.

## B. Determinantal quantum Monte Carlo computation

We follow a lattice Hamiltonian formulation, somewhat different from the Lagrangian formulation usually used in lattice QCD [38]. Instead of using the representation in terms of coherent-state Grassmann variables, we use the number representation, working with the lattice Fock space  $\langle n|$  using the creation and annihilation operators of the neutrons. Our treatment is the same as that used in Refs. [21, 34, 39] and is commonly used in condensed-matter physics [19, 20] under the determinantal quantum Monte Carlo (DQMC) method.

We carry out neutron matter calculations using the Hamiltonian of Eq. (5) in the method of grand canonical ensemble. The Monte Carlo computation is carried out for various values of the chemical potential  $\mu$ , and the  $\mu$  dependence is converted to the density dependence by determining the densities by the average over  $i, \sigma$  of  $\langle \hat{c}_{i\sigma}^\dagger \hat{c}_{i\sigma} \rangle$  for various values of  $\mu$ .

For many-nucleon systems, the Hamiltonian (5) should also include three-nucleon interactions. By EFT power counting rules, the interactions are to be treated generally as the

LO order in the pionless case, and they play a significant role when a three-nucleon bound state such as the triton can be formed [40]. In neutron matter, however, the three-neutron system has no bound state, and the three-neutron interactions appear at a higher order because the Fermi statistics prohibit the LO diagram of three neutron from being at the same spatial point with the momentum-independent vertex. As the interactions would also affect the two-neutron pairing indirectly, we expect that the interactions would affect the observables of our interest relatively weakly and defer the issue to a future investigation by neglecting them in this work.

We write the partition function as

$$\mathcal{Z}(T, \mu) \equiv \langle n | \hat{U}(\beta) | n \rangle, \quad (7)$$

where  $\hat{U}(\beta)$  is the (imaginary time) evolution operator, and the trace implied in Eq. (7) is over all possible nucleon configurations on the lattice  $\langle n |$ . Using the Trotter-Suzuki approximation, we express  $\hat{U}(\beta)$  as

$$\hat{U}(\beta) = \mathcal{T} \exp \left[ - \sum_{\tau_t=1}^{N_t} \Delta\beta \left( \hat{H} - \mu \sum_{i\sigma} \hat{c}_{i\sigma}^\dagger \hat{c}_{i\sigma} \right) \right] \equiv \mathcal{T} \Pi_{\tau_t=1}^{N_t} \hat{U}(\Delta\beta) \quad (8)$$

by the temporal discretization  $\beta = \Delta\beta N_t$ , with  $N_t$  being the number of time slices. In Eq. (8),  $\hat{H}$  is the two-parameter NLO Hamiltonian of Eq. (5), and  $i$  is actually an integer vector specifying the location of a site with its component ranging as  $[-aN_s^{1/3}/2, aN_s^{1/3}/2]$ . The  $\tau_t$  dependence of  $\hat{H}$  and  $\hat{U}(\Delta\beta)$  is solely through  $\hat{c}^\dagger$  and  $\hat{c}$ , as seen from Eq. (5). The last expression in Eq. (8) is thus a product of  $\hat{U}(\Delta\beta)$  operators, each having the same form and depending on  $\tau_t$  implicitly.

To cast  $\mathcal{Z}(T, \mu)$  in a form amenable to Monte Carlo computation of the fermion integration, we express the two-nucleon interaction of  $\hat{H}$  in a single-nucleon interaction form by applying the Hubbard-Stratonovich transformation

$$e^{+A\hat{n}_i^2} = \sqrt{\frac{A}{\pi}} \int d\chi_i e^{-A(\chi_i^2 - 2\chi_i\hat{n}_i)} \quad (9)$$

for a constant  $A$  with  $\text{Re}(A) > 0$ . Here,  $\chi_i$  is an auxiliary scalar field at the  $i$ th site, and  $\hat{n}_i$  is the density operator defined as  $\hat{n}_i \equiv \hat{n}_{i\uparrow} + \hat{n}_{i\downarrow}$  ( $\hat{n}_{i\sigma} \equiv \hat{c}_{i\sigma}^\dagger \hat{c}_{i\sigma}$ , the number operator with the spin  $\sigma$  at the  $i$ th site).  $\hat{H}$  is divided into two parts,

$$\hat{H} \equiv \left[ \hat{H}_s + \frac{1}{2a^3} c_0^{(0)}(a) \sum_i \hat{n}_i^2 \right] + \hat{H}', \quad (10)$$



where

$$\begin{aligned}\hat{H}_s &\equiv -t \sum_{\langle i,j \rangle \sigma} \hat{c}_{i\sigma}^\dagger \hat{c}_{j\sigma} + \left[ 6t - \frac{1}{2a^3} c_0^{(0)}(a) \right] \sum_i \hat{n}_i \\ \hat{H}' &\equiv \frac{1}{2a^5} c_2(a) \sum_{\langle i,j \rangle} \hat{n}_i \hat{n}_j + \frac{1}{2a^3} \left[ \Delta c_0(a) - \frac{6}{a^2} c_2(a) \right] \sum_i (\hat{n}_i^2 - \hat{n}_i).\end{aligned}\quad (11)$$

Here,  $c_0(a)$  is expressed as a sum of the LO part  $c_0^{(0)}(a)$  and the NLO part  $\Delta c_0(a)$ , which are defined in Eqs. (A3) and (A2), respectively, with  $\Lambda = \pi/a$ .

We introduce  $\hat{H}_0(\chi)$ , the LO single-nucleon Hamiltonian interacting with the external scalar field  $\chi \equiv \{\chi_i\}$ ,

$$\hat{H}_0(\chi) \equiv \hat{H}_s + \frac{1}{a^3} c_0^{(0)}(a) \sum_i \chi_i \hat{n}_i. \quad (12)$$

In terms of  $\hat{H}_0(\chi)$ ,  $\hat{U}(\Delta\beta)$  is written as

$$\begin{aligned}\hat{U}(\Delta\beta) &= \int d[\chi] \exp \left[ + \frac{\Delta\beta}{2a^3} c_0^{(0)}(a) \sum_i \chi_i^2 \right] \exp \left\{ -\Delta\beta \left[ \hat{H}_0(\chi) + \hat{H}' - \mu \sum_i \hat{n}_i \right] \right\} \\ &\approx \int d[\chi] e^{+\frac{\Delta\beta}{2a^3} c_0^{(0)}(a) \sum_i \chi_i^2} (1 - \Delta\beta \hat{H}') e^{-\Delta\beta [\hat{H}_0(\chi) - \mu \sum_i \hat{n}_i]},\end{aligned}\quad (13)$$

where the measure is defined as  $d[\chi] \equiv d\chi_1 d\chi_2 \dots$  with a constant factor generated by the Hubbard-Stratonovich transformation. We emphasize that  $\hat{H}'$  is defined to be of the NLO and is treated perturbatively in the second step of Eq. (13).

We thus obtain

$$\begin{aligned}\mathcal{Z}(T, \mu) &\approx \int d[\chi] \mathcal{T} \Pi_{\tau_t=1}^{N_t} e^{+\frac{\Delta\beta}{2a^3} c_0^{(0)}(a) \sum_i \chi_i^2} \langle n | (1 - \Delta\beta \hat{H}') e^{-\Delta\beta [\hat{H}_0(\chi) - \mu \sum_i \hat{n}_i]} | n \rangle \\ &\equiv \int d[\chi] G(\chi) \langle n | \hat{U}_\chi(\beta) | n \rangle,\end{aligned}\quad (14)$$

where

$$\begin{aligned}G(\chi) &\equiv \Pi_{\tau_t=1}^{N_t} e^{+\frac{\Delta\beta}{2a^3} c_0^{(0)}(a) \sum_i \chi_i^2} \\ \hat{U}_\chi(\beta) &= \Pi_{\tau_t=1}^{N_t} \hat{U}_\chi(\Delta\beta) \equiv \Pi_{\tau_t=1}^{N_t} (1 - \Delta\beta \hat{H}') e^{-\Delta\beta [\hat{H}_0(\chi) - \mu \sum_i \hat{n}_i]}.\end{aligned}\quad (15)$$

Note that the time-ordering (sequential) integration over  $[\chi]$  is understood in the last expression of Eq. (14). In accordance with Eq. (13), the factor  $(1 - \Delta\beta \hat{H}')$  in  $\hat{U}_\chi(\Delta\beta)$  of Eq. (15) is to be evaluated by the use of the nucleon lattice configuration resulting from the  $\exp\{-\Delta\beta [\hat{H}_0(\chi) - \mu \sum_i \hat{n}_i]\}$  operation at  $\tau_t$ , and that this procedure is repeated successively

from  $\tau_t = 0$  to  $N_t$ . This step is vital in the computation for the perturbative treatment of  $\hat{H}'$ . We make a technically important note: because of the perturbative treatment of  $\hat{H}'$ , the number of the auxiliary fields for the NLO calculation remains as  $N_s N_t$ , the same as for the LO calculation. If  $\hat{H}'$  were not treated perturbatively,  $4 \times N_s N_t$  more of  $\{\chi_i\}$  would have been needed owing to the derivative interactions, and the Monte Carlo computation would have required more time by nearly an order of magnitude.

The trace of the single-particle evolution operator  $\hat{U}_\chi(\beta)$  is expressed in terms of the single-particle matrix representation of the operator,  $\mathbf{U}_\chi(\beta)$ , as [19, 20, 21, 39]

$$\langle n | \hat{U}_\chi(\beta) | n \rangle = \det [1 + \mathbf{U}_\chi(\beta)] \equiv \xi(\chi). \quad (16)$$

The expectation value of the (static) operator  $\mathcal{O}(\hat{c}^\dagger, \hat{c})$  at  $T = 1/\beta$  is then obtained from

$$\begin{aligned} \langle \mathcal{O}(\hat{c}^\dagger, \hat{c}) \rangle &= \frac{1}{\mathcal{Z}(T, \mu)} \int d[\chi] G(\chi) \langle n | \mathcal{O}(\hat{c}^\dagger, \hat{c}) \hat{U}_\chi(\beta) | n \rangle \\ &\equiv \frac{\int d[\chi] G(\chi) \langle \mathcal{O}(\chi) \rangle \xi(\chi)}{\int d[\chi] G(\chi) \xi(\chi)}, \end{aligned} \quad (17)$$

where  $\langle \mathcal{O}(\chi) \rangle$  is

$$\langle \mathcal{O}(\chi) \rangle \equiv \frac{\langle n | \mathcal{O}(\hat{c}^\dagger, \hat{c}) \hat{U}_\chi(\beta) | n \rangle}{\langle n | \hat{U}_\chi(\beta) | n \rangle} \quad (18)$$

and can be evaluated in terms of  $\mathbf{U}_\chi(\beta)$  using Eq. (16), as shown in Refs. [19, 20, 21, 39].

Equation (17) is now amenable to a Monte Carlo integration by treating  $|G(\chi)|$  or  $|G(\chi)\xi(\chi)|$  as a weight. Our Monte Carlo computation is the same as that used in Ref. [21], supplemented by a matrix-decomposition stabilized method for low-temperature computations [19, 20].

Before closing this subsection, we make a relevant comment. In the procedure just described, we reduced the original Hamiltonian  $\hat{H}$  of Eq. (5) to the single-nucleon Hamiltonian  $\hat{H}_0$  (with  $\hat{H}'$ ) of Eq. (12) in terms of the density operators  $\{\hat{n}_i\}$ , as in Eq. (10). The choice of the density operators in this step may seem natural, but it is not required for the reduction to an effective single-nucleon Hamiltonian because of the arbitrariness in the path integral formulation. In fact, we can choose a combination of pairing operators and density operators, leading to a Hartree-Fock-Bogoliubov (HFB) type Hamiltonian [39, 41].

### C. Lattice spacing toward thermodynamic and continuum limits

Neutron matter is a strongly correlated fermion system. On a three-dimensional cubic lattice, the correlation length resulting from the simulation,  $\xi$ , satisfies

$$a \ll \xi \lesssim L, \quad (19)$$

where  $L \equiv aN_s^{1/3}$  is the physical dimension of the cubic lattice.  $\xi$  is the length scale in which the collective state is realized in the simulation and is different from the size of a neutron pair (a Cooper pair) in the state  $\xi_{\text{cp}}$ . Note that, confusingly,  $\xi_{\text{cp}}$  has often been referred to terms similar to  $\xi$ . In Appendix B, we compare the physical sizes of the neutron pair simulated and the lattice spaces used.

To obtain a physically meaningful result, we seek for  $\xi$  and for the expectation values of other quantities, in the continuum limit  $a \rightarrow 0$  and in the thermodynamic limit  $L \rightarrow \infty$ . The clear procedure for achieving both limits is to do the former with  $L$  fixed (for obtaining results insensitive to the lattice structure), and then to do the latter (using finite volume corrections), as is usually done in lattice QCD calculations [38].

In our calculation of the many neutron system, each meaningful configuration must consist of neutrons fewer than  $N_s$ , so that the calculation properly describes the interacting neutron system *in free space*. This requirement is crucial in general for the simulation of a system of many fermions, and we find that the requirement complicates the straightforward approach of achieving the above two limits. Note that lattice QCD calculations have not yet dealt with cases of such high baryon-density states.

Let us elaborate on this requirement. Consider setting up a classical lattice configuration. When  $N_f$  neutrons are placed on a lattice of volume  $a^3 N_s$ , the neutron density  $\rho$  is

$$\rho \equiv \frac{N_f}{N_s a^3} \equiv \frac{n}{a^3}, \quad (20)$$

which defines the lattice-filling fraction (or more descriptively, the site-occupation fraction),  $n \equiv N_f/N_s$ .  $n$  denotes the fraction of the lattice sites occupied by the neutrons. Note that the complete filling of the lattice occurs with  $n = 2$  owing to the spin degree of freedom. Classically,  $n$  can simply be chosen, while in our quantum-mechanical, grand canonical calculation, it is determined from  $\sum_{i,\sigma} \langle \hat{c}_{i\sigma}^\dagger \hat{c}_{i\sigma} \rangle$ , which is computed for a fixed value of  $a$  and  $\mu$ .

Mathematically, for a finite nucleon density, Eq. (20) implies

$$n(\mu) \rightarrow 0 \quad (21)$$

as  $a \rightarrow 0$ . Physically, these limits simulate the free-space environment, because the smaller  $n$  is, the more vacant sites are available, allowing more feasible excitations to be realized. To determine thermal quantities as a function of neutron matter density, we consider achieving the limits to be vital and take the limit of Eq. (21) as the continuum limit. Note that this procedure is similar to, but different from, the one recently proposed for the unitary limit problem [42], in that we keep the density  $\rho$  finite as we approach the continuum limit, but the  $k_F \rightarrow 0$  limit is taken in Ref. [42].

Once we decide to take Eq. (21) as the continuum limit, we have to use different values of  $a$  for different densities to satisfy the regularization scale requirement, Eqs. (3) and (4), of the EFT. The procedure becomes complicated in order to satisfy all these requirements, but at the same time it has to be durable in practice. We have decided to use the following procedure. First, we choose an appropriate  $n$  value that is small enough yet reasonably durable. Second, for this  $n$ , we choose a set of the representative nucleon densities for the computation and a set of appropriate  $a$  values for them. We call the set the standard parameter set, and we list them in Sec. II D. Third, after we complete the computation for the standard set, we perform the computation by varying the lattice size, so as to take the thermodynamic limit. Fourth, we vary  $n$  to examine the continuum limit as  $n \rightarrow 0$ .

In the rest of this subsection, we discuss the first step, how we choose  $n$  for the standard set. As an estimate, take the Fermi gas model. In terms of the Fermi momentum  $k_F$ ,  $n$  for neutron matter is written as

$$n = (ak_F)^3 / (3\pi^2) \rightarrow 0. \quad (22)$$

To keep  $n$  independent of  $a$  for various densities, we should have  $a \propto 1/k_F$ . Note that the excitation energies of the neutron matter of interest are about an order of magnitude less than the Fermi energy, as seen in Sec. V, and are safely ignored in this estimate.

The smallness of  $n$  is achieved by making  $a$  small, or  $\Lambda$  large. If we take Eq. (3), Eq. (2) with  $p \sim k_F$  yields

$$\pi > ak_F. \quad (23)$$

Equations (22) and (23) yield a rather loose estimate of  $n < 1$ . We can obtain a more realistic

limit from the observation that the lattice discretization amounts to the replacement

$$\mathbf{p}^2 \rightarrow \frac{2}{a^2} \sum_{i=1}^3 [1 - \cos(ap_i)] = \mathbf{p}^2 + \mathcal{O}(a^2 \mathbf{p}^4), \quad (24)$$

for example, in the neutron propagator. This observation suggests that the left-hand side of Eq. (23) is more like unity instead of  $\pi$ , and we obtain the inequality

$$(3\pi^2)^{-1/3} > n. \quad (25)$$

This choice of  $n$  does not require a large  $\Lambda$  to satisfy Eq. (4), but it does for Eq. (3).

The preceding consideration leads us to set  $n = 1/4$  (or  $1/8$  of the full filling of the lattice), as a practical compromise. Other parameters also need to be chosen. In the following subsection, we discuss how they are chosen and list all parameter values in the standard parameter set.

#### D. Standard parameter set

The standard set of the potential parameters is shown in Table I. We choose the set by the following steps. First, we choose the values of the Fermi momentum  $k_F$ , representing the neutron matter density, as shown in the first and second columns. Second, the values of  $a$  are determined from  $(ak_F)^3/(3\pi^2) = n = 1/4$  and at the same time by ensuring that the  $a$  values provide reasonable EFT regularization scales. Third, the values of  $c_0$  and  $c_2$  are determined from  $a_0$  and  $r_0$  using the  $a$  values in Eqs. (A2) and (A3) with  $\Lambda = \pi/a$ . The Monte Carlo calculations are carried out using the  $c_0$  and  $c_2$  values by tuning the chemical potential  $\mu$ , so that the resultant neutron matter densities by the Monte Carlo computation are the  $\rho$  values listed in the third column in the unit of the normal nuclear density  $\rho_0 = 0.16 \text{ fm}^{-3}$ . We emphasize that these  $\rho$  values are expressed in terms of the  $k_F$  values in the first and second column exactly as

$$\rho = k_F^3/(3\pi^2). \quad (26)$$

Throughout this work, we use  $k_F$  defined through Eq. (26) for specifying the *quantum-mechanically computed density*,  $\rho$ , of neutron matter as the interacting fermion system.

TABLE I: Standard parameter set.

	$k_F$ (MeV)	$k_F$ (fm $^{-1}$ )	$\rho$ ( $\rho_0$ )	$a$ (fm)	$c_0/(a^3t)$	$c_2/(a^5t)$
LO	15	0.07602	$9 \times 10^{-5}$	25.64	-5.308	–
LO	30	0.1520	$7 \times 10^{-4}$	12.82	-6.354	–
LO	60	0.3041	$6 \times 10^{-3}$	6.409	-7.049	–
NLO	60	0.3041	$6 \times 10^{-3}$	6.409	-9.646	0.3684
NLO	90	0.4561	$2 \times 10^{-2}$	4.273	-11.074	0.5139
NLO	120	0.6081	$5 \times 10^{-2}$	3.205	-12.343	0.6555

### III. DETERMINATION OF $\Delta$ , $T_c$ , AND $T^*$ FROM THE PAIRING CORRELATION FUNCTION

In this work, we focus on the determination of three quantities: the  $^1S_0$  pairing gap at  $T \approx 0$ ,  $\Delta$ ; the critical temperature  $T_c$  of the normal-to-superfluid phase transition; and the pairing temperature scale  $T^*$ . The latter two will be used to obtain the density-temperature phase diagram, and all quantities will be calculated from correlation functions, the first two from the pair-pair correlation function and the third from the magnetic susceptibility (the spin-spin correlation).

#### A. Pairing gap $\Delta$

$\Delta$  is determined directly from the off-diagonal long-range order (ODLRO) of the spin pair-pair correlation function  $P_s$  [43],

$$\begin{aligned}
 P_s(R) &= \frac{1}{N_s} \sum_i \langle \hat{\Delta}_{i+R}^\dagger \hat{\Delta}_i \rangle \\
 &= \frac{1}{N_s} \sum_{i, j=i+R} (\delta_{ij} - G_{ji})^2,
 \end{aligned} \tag{27}$$

where  $\hat{\Delta}_i \equiv \hat{c}_{i\uparrow}\hat{c}_{i\downarrow}$  is the two-neutron spin-pairing operator at the  $i$ th site, and  $R$  is the separation of the neutron pairs in the lattice spacing unit and has no dimension. Note that  $G_{ij} \equiv G_{ij}^\sigma = \langle \hat{c}_{i\sigma}\hat{c}_{j\sigma}^\dagger \rangle$  for  $\sigma = \uparrow, \downarrow$  in the attractive Hubbard model.  $P_s(R)$  decays rapidly in  $R \approx 1$  or 2 and takes a diminishing asymptotic value. When a long-range order exists

between neutron pairs, the asymptotic value is finite, that is, the signature of the ODLRO. Figure 1 illustrates this behavior.

In Fig. 1,  $P_s(R)$  is calculated for 14 values of  $T/t$  between 2.0 and 0.0625; but for clarity, only the selected values of  $T/t$  are shown. Note that the integer points of  $R = 1-4$  arise from the lattice points in the side of the cubic, while the largest  $R = 4\sqrt{3} \approx 7$  comes from the midpoint of the diagonal line in the cubic, which has the displacement vector  $\langle 4, 4, 4 \rangle$ . The values for  $R \geq 3$  are found to be quite close to each other at the lowest three temperatures,  $T/t = 0.25$ , 0.125, and 0.0625. The values at  $R = 4$  and 7 are averaged, yielding  $P_s(T \approx 0, R \gg 1)$ .  $\Delta$  is then determined from

$$\Delta = \frac{|c_0|}{a^3} \sqrt{P_s(T \approx 0, R \gg 1)}. \quad (28)$$

Similar procedures are applied for different  $N_s$  and  $k_F$ . The errors from the fit hereafter are estimated by a constrained least-squares method.

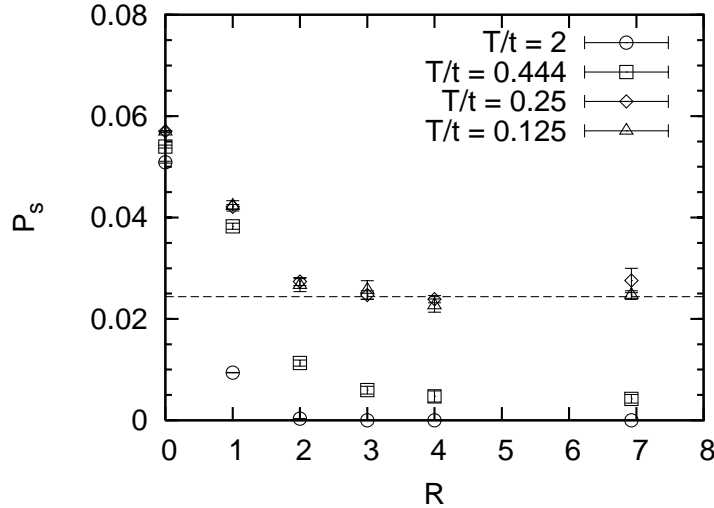


FIG. 1: Spin pair-pair correlation function  $P_s$  as a function of the lattice separation  $R$  for the lattice size  $N_s = 8^3$  for the site-occupation fraction  $n = 0.25$  at  $k_F = 30$  MeV. The DQMC results are shown with statistical uncertainties for  $T/t = 2.0$ , 0.444, 0.25, and 0.125 in the unit of hopping amplitude  $t = 0.126$  MeV. The dashed line is the asymptotic value of  $P_s = 0.0244(6)$  extracted from the values for  $R = 4$  and  $4\sqrt{3}$  at  $T/t = 0.25$ , 0.125, and 0.0625 (not shown).

Note that, as seen in Fig. 2 of the next subsection, the critical temperature is  $T_c/t = 0.335(1)$ , and the behavior of  $P_s(R)$  at  $T_c$  is similar to  $T/t = 0.25$  in Fig. 1. We caution the

reader that the  $\Delta$  thus determined is not our final value but is the value for  $N_s = 8^3$  and  $n = 1/4$  at  $k_F = 30$  MeV. Using  $\Delta$ 's for various values of  $N_s$  and  $n$  at each  $k_F$ , we determine  $\Delta$  at the thermodynamic and continuum limits by the further analysis described in Sec. IV. The same caution is applied to the determination of  $T_c$  and  $T^*$  in the following subsections.

### B. Critical temperature $T_c$

$T_c$  of the normal-to-superfluid phase transition is determined from the spin pair-pair correlation sum [44, 45, 46, 47]

$$\begin{aligned} C_\Delta(T) &= \frac{1}{N_s} \sum_{i,j} \langle \hat{\Delta}_i \hat{\Delta}_j^\dagger + \hat{\Delta}_i^\dagger \hat{\Delta}_j \rangle \\ &= \frac{1}{N_s} \sum_{i,j} [(G_{ij})^2 + (\delta_{ij} - G_{ji})^2]. \end{aligned} \quad (29)$$

$T_c$  is extracted from the inflexion point of  $C_\Delta(T)$ . Figure 2 illustrates a typical case of  $C_\Delta$  as a function of  $T/t$ , for  $k_F = 30$  MeV and  $N_s = 8^3$ . In the figure, the inflexion point is at  $T_c/t = 0.335(1)$ , or  $T_c = 0.0423(1)$  with  $t = 0.1261$  MeV. The inflexion point is determined by an interpolation that fits the Monte Carlo data with an assumed function,

$$C_\Delta(T) = -C_1 \tanh[C_2(T - T_c)/t] + C_3, \quad (30)$$

where  $C_1 = C_\Delta(T = 0)/2$ ,  $C_2$ , and  $C_3$  are free constant parameters.

### C. Pairing temperature Scale $T^*$

As the temperature increases, the long-range order of the superfluidity disappears at  $T_c$ . Above  $T_c$ , the spin pairing still remains, however, without generating the long-range order, and as the temperature increases further, the pairing eventually disappears. Though the process of the pairing disappearance is expected to be a continuous process, we may identify the temperature below which the pairing can be viewed as still strong. Following a practice in condensed-matter physics [46, 47], we denote the temperature as the pairing temperature scale  $T^*$  and determine it from the temperature dependence of the Pauli spin susceptibility  $\chi_P$ . When the (*S*-wave singlet) spin pairing is weakened, the spectral weight of low-energy spin excitations is reduced, and the spin response weakens.  $\chi_P$  is a good



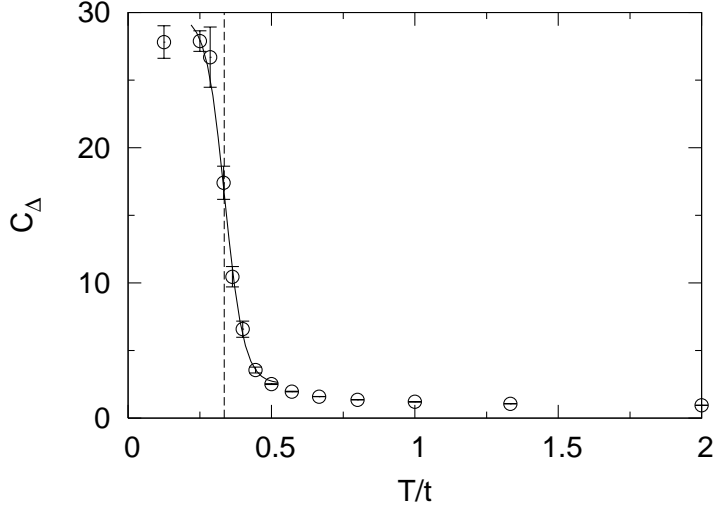


FIG. 2: Spin pair-pair correlation sum  $C_\Delta$  as a function of temperature  $T$  in the unit of the hopping parameter  $t$ . The Monte Carlo data with the statistical uncertainties are shown for the case of  $N_s = 8^3$  and  $k_F = 30$  MeV. The vertical dashed line signifies  $T_c(N_s = 8^3) = 0.335(1)t$ , corresponding to the inflexion point of the interpolated curve of  $C_\Delta(T/t)$ , Eq. (30) with  $C_1 = 13.6 \pm 1.0$ ,  $C_2 = 15.1 \pm 2.9$ , and  $C_3 = 16.2 \pm 0.6$ . The interpolated curve is shown as the solid curve.

quantity for studying this transition, since the  $\chi_P$  of a free fermion gas diverges as  $T \rightarrow 0$ , while it vanishes for an interacting fermion gas, as illustrated in Fig. 3.

$\chi_P$  is given by

$$\begin{aligned}\chi_P(T, N_s) &= \frac{1}{T} \frac{1}{N_s} \sum_{i,j} \langle \mathbf{S}_i \cdot \mathbf{S}_j \rangle \\ &= \frac{1}{T} \frac{1}{N_s} \sum_{i,j} 2G_{ij} (\delta_{ij} - G_{ji}),\end{aligned}\tag{31}$$

where  $\mathbf{S}_i = \sum_{\mu,\nu=\uparrow,\downarrow} c_{i\mu}^\dagger \boldsymbol{\sigma}_{\mu\nu} c_{j\nu}$  and  $\boldsymbol{\sigma}$  is the Pauli vectorial matrices.  $T^*$  is determined by identifying the maximum point of  $\chi_P$  as a function of  $T$  [46, 47], as discussed in the following.

Figure 4 shows a typical case. For  $k_F = 30$  MeV and  $N = 8^3$ , we obtain  $T^*/t = 0.5253(3)$  [ $T^* = 0.06624(3)$  MeV with  $t = 0.1261$  MeV]. The maximum point of the Monte Carlo data is determined through interpolation by use of a fitting function with a parameter  $C_1$ ,

$$\chi_P(T) = C_1 T \exp(-T/T^*).\tag{32}$$

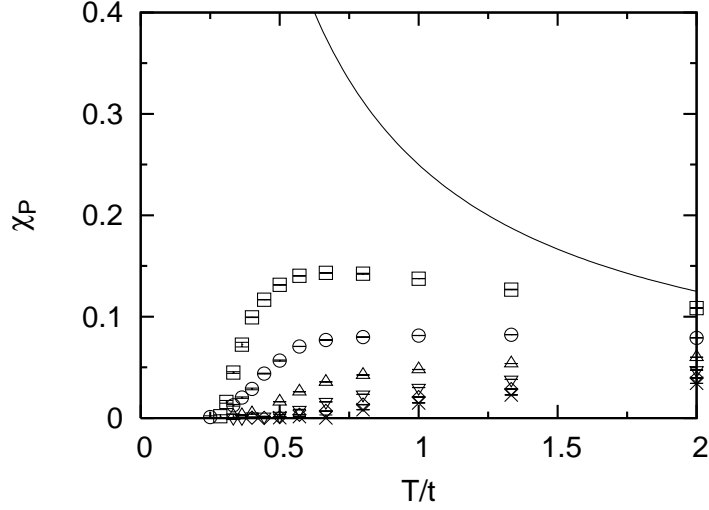


FIG. 3: Pauli spin susceptibility  $\chi_P$  as a function of temperature  $T$  in the unit of hopping parameter  $t$  for  $N_s = 4^3$ . The solid curve is the free fermion gas limit ( $|c_0|/(a^3 t) \rightarrow 0$ ) of  $\chi_P(T)$ ,  $\approx n(1-n/2)/T$  (with the filling fraction  $n$ ) [48]. In comparison to this, the cases for  $|c_0|/(a^3 t) = 2, 4, 6, 8, 10$ , and  $12$  are shown in the increasing order of the interaction strength, from top to bottom.

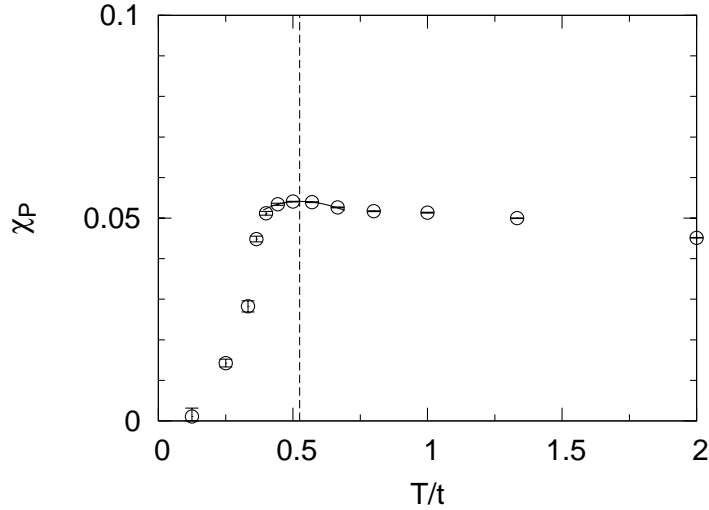


FIG. 4: Pauli spin susceptibility  $\chi_P$  as a function of temperature  $T$  in the unit of hopping parameter  $t$  for  $N_s = 8^3$  and  $k_F = 30$  MeV. The vertical dashed line signifies  $T^*(N_s = 8^3) = 0.5253(3)t$ , which is determined as the maximum point of  $\chi_P(T)$ , using the fitting function Eq. (32) with  $C_1 = 0.258 \pm 0.008$  (shown as the solid curve).

Note that though the definition of  $T^*$  is somewhat subjective,  $T^*$  thus defined approaches  $T_c$  at the BCS limit, and  $T^*$  signifies the pair-forming temperature at the BEC limit as  $T^* \propto |c_0|/[a^3 t \ln(|c_0|/(a^3 t \epsilon_F))^{3/2}]$  [28, 47]. Here, the BCS and BEC limits correspond to the weak and strong interaction limits, or the small and large  $c_0/(a^3 t)$  limits, respectively.

#### IV. $\Delta$ , $T_c$ , AND $T^*$ AT THE THERMODYNAMIC AND CONTINUUM LIMITS

##### A. Pairing gap $\Delta$

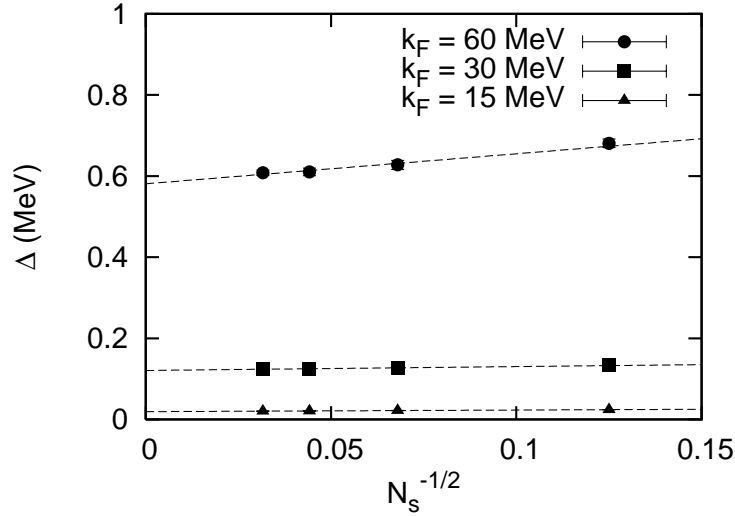


FIG. 5: Lattice-size ( $N_s$ ) dependence of  $\Delta$  at LO for  $k_F = 15, 30$ , and  $60$  MeV with  $n = 1/4$ . The Monte Carlo data shown with the statistical uncertainties are obtained for  $N_s = 4^3, 6^3, 8^3$ , and  $10^3$ . The dashed lines are the best fits by the use of linear functions of  $N_s^{-1/2}$ .

As the first step, we determine  $\Delta$  at the thermodynamic limit. To carry out a definite analysis, we apply the BCS finite-size scaling exponent,  $\lambda = 3/2$  in  $\Delta \sim L^{-\lambda} = N_s^{-\lambda/3}$  as being independent of the density [49]. The exponent is obtained through  $\Delta(T = 0, N_s) \propto T_c(N_s) \sim L^{-3/2} = N_s^{-1/2}$  by combining the BCS result,  $\Delta(T = 0) \approx 1.76T_c$ , and the direct relations between the finite-size scaling and critical exponents [49, 50]. Note that while the usual  $\chi^2$  best fit to all of our Monte Carlo data results in an essentially indefinite  $\lambda$ , the jackknife method (often used in the lattice QCD data analysis [38]) yields  $\lambda = 1.6 \pm 0.3$  by assuming a linear  $L^{-\lambda}$  dependence independent of the density. Apparently the value of

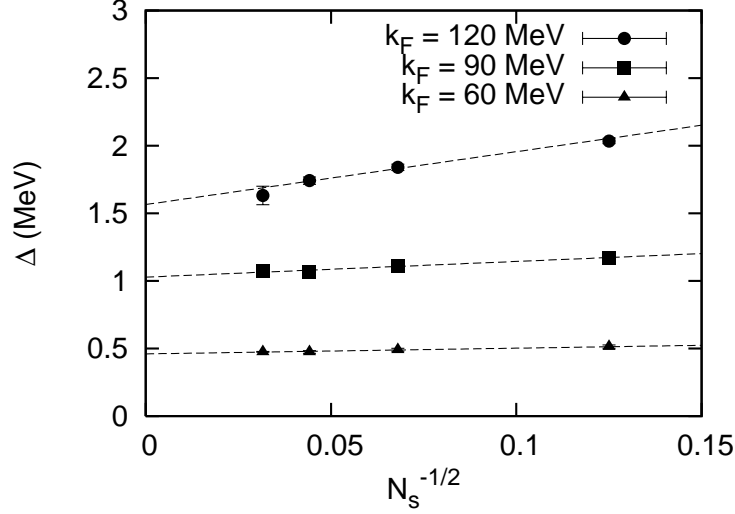


FIG. 6: Same as Fig. 5, but at NLO for  $k_F = 60, 90$ , and  $120$  MeV.

the exponent changes little between the BCS weak-coupling region and the neutron-matter BCS-BEC crossover region. Figures 5 and 6 show the choice of  $\lambda = 3/2$  reasonable.

In Figs. 5 and 6, the finite-size scaling of  $\Delta$  is shown as a function of  $N_s$  using  $N_s = 4^3, 6^3, 8^3$ , and  $10^3$  data with  $n = 1/4$ . Fig. 5 is the finite-size scaling of  $\Delta$  evaluated at LO for  $k_F = 15, 30$ , and  $60$  MeV, while Fig. 6 is at NLO for  $k_F = 60, 90$ , and  $120$  MeV. The data at LO are found to be best fit with a linear dependence on  $N_s^{-1/2} = L^{-3/2}$  as

$$\begin{aligned}
\Delta(N_s, k_F = 15 \text{ MeV}) &= 0.0394(34) N_s^{-1/2} + 0.019152(20), \\
\Delta(N_s, k_F = 30 \text{ MeV}) &= 0.096(35) N_s^{-1/2} + 0.1207(16), \\
\Delta(N_s, k_F = 60 \text{ MeV}) &= 0.74(24) N_s^{-1/2} + 0.581(13),
\end{aligned} \tag{33}$$

and those for NLO are

$$\begin{aligned}
\Delta(N_s, k_F = 60 \text{ MeV}) &= 0.423(67) N_s^{-1/2} + 0.4602(54), \\
\Delta(N_s, k_F = 90 \text{ MeV}) &= 1.16(17) N_s^{-1/2} + 1.028(14), \\
\Delta(N_s, k_F = 120 \text{ MeV}) &= 3.91(75) N_s^{-1/2} + 1.565(42),
\end{aligned} \tag{34}$$

where the last constant for each value of  $k_F$  is  $\Delta$  at the thermodynamic limit ( $N_s \rightarrow \infty$ ). The best-fit constants in Eqs. (33) and (34) are determined using the jackknife method.

As the second step, we determine  $\Delta$  in the continuum limit using the above thermodynamic limit values. As discussed in Sec. II C, these values are obtained by using the standard

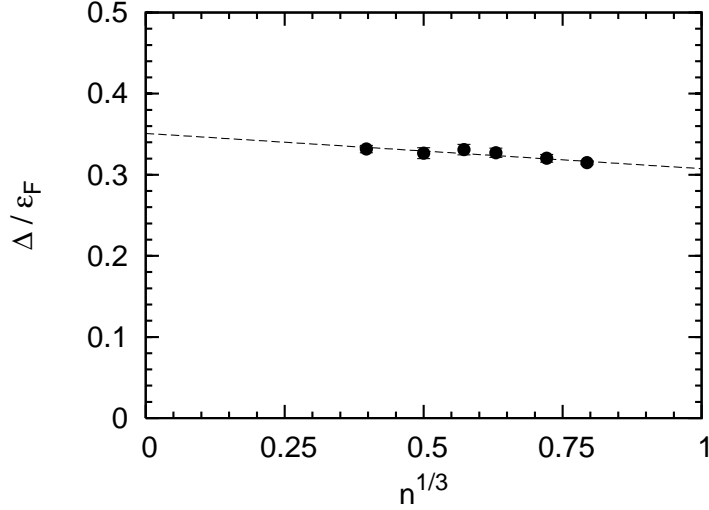


FIG. 7: Pairing gap  $\Delta$  in the unit of the Fermi energy  $\epsilon_F$  as a function of the filling fraction  $n$  for  $k_F = 60$  MeV. The solid circles show Monte Carlo data for  $N_s = 6^3$  at LO, with statistical uncertainties. The dashed line is the best fit by the use of a linear  $n^{1/3}$  dependence. The interception of the dashed line with the vertical axis corresponds to  $\Delta$  at the continuum limit ( $n \rightarrow 0$ ) for  $N_s = 6^3$  at  $k_F = 60$  MeV.

parameter set, or with  $n = 1/4$  (half of the quarter-filling), and are needed to extrapolate to  $n = 0$  to reach the continuum limit,  $a \rightarrow 0$ . For the extrapolation, we need to know how much  $\Delta$  changes between  $n = 1/4$  and  $n \rightarrow 0$ , or the ratio of  $\Delta$  at the two values of  $n$ ,  $R_\Delta$ . In this work, we determine  $R_\Delta$  solely using LO Monte Carlo data of the  $N_s = 6^3$  lattice for  $k_F = 60$  MeV. Dependence of  $R_\Delta$  on  $N_s$  and  $k_F$  is weak both for LO and NLO, as discussed in Sec. IV D.

Figure 7 shows the dependence of  $\Delta$  on  $n$  for  $N_s = 6^3$  at  $k_F = 60$  MeV. The data in the figure, shown with statistical uncertainties by solid circles, are for  $n = 1/16, 1/8, 3/16, 1/4, 3/8$ , and  $1/2$ . The EFT potential parameter  $c_0(a)$  is varied by the use of Eq. (A3) to accommodate the variation of  $a$  generated by the change of  $n$ .

The  $n$  dependence of  $\Delta$  is found to be relatively weak, and the jackknife analysis of the data yields

$$\Delta(n, N_s = 6^3)/\epsilon_F = -0.07(7) n^{1.6(1.3)} + 0.337(20). \quad (35)$$

While more data are desirable to reduce the uncertainty of the continuum limit, the constant term in Eq. (35), some indirect information of the  $n$  exponent is available from the weak-

coupling BCS theory by the use of  $\Delta \propto T_c$ , and also from the analysis by Burovski *et al.* [42] in a similar limit (but with  $k_F \rightarrow 0$  as noted in Sec. II C) for their unitary limit calculation. Both suggest the  $n^{1/3}$  dependence, with which we find the best fit

$$\Delta(n, N_s = 6^3)/\epsilon_F = -0.044(16) n^{1/3} + 0.351(10). \quad (36)$$

For definiteness and because of lack of time, we use in our present analysis Eq. (36) and show it as the dashed line in Fig. 7. Equations (35) and (36) yield the statistically consistent  $\Delta$  at the continuum limit and suggest the systematic uncertainty by the use of the  $n^{1/3}$  dependence to be several percent.

Equation (36) gives the ratio  $R_\Delta$

$$R_\Delta \equiv \frac{\Delta(n \rightarrow 0, N_s = 6^3)}{\Delta(n = 0.25, N_s = 6^3)} = \frac{0.674(19) \text{ MeV}}{0.628(11) \text{ MeV}} = 1.07(5). \quad (37)$$

That is, the continuum-limit correction amounts to a 7% increase in the value of  $\Delta$ . Exploiting the weak dependence of  $R_\Delta$  on  $N_s$  and  $k_F$  (elaborated in Sec. IV D), we apply the same  $R_\Delta$  to  $\Delta$  at the thermodynamic limit in Eqs. (33) and (34), so as to obtain the final values of  $\Delta$  at the thermodynamic and continuum limits.

## B. Critical temperature $T_c$ and pairing temperature scale $T^*$

To obtain  $T_c$  and  $T^*$  at the thermodynamic and continuum limits, we carry out the same two steps as those done on  $\Delta$  in the preceding subsection. Because  $T_c$  is at criticality, we will apply the universality argument for taking the thermodynamic limit. Monte Carlo data at  $n = 1/4$  used for the finite-size scaling of  $T_c$  and  $T^*$  are shown in Figs. 8 and 9 for  $N_s = 4^3, 6^3, 8^3$ , and  $10^3$  with statistical uncertainties.

The exponent of the finite-size scaling and the critical exponents are known to be directly related at criticality [50]. Furthermore, because the three-dimensional (3D) XY model and our 3D Hubbard model are expected to belong to the same universality class [47, 49, 51], the exponents of finite-size scaling at criticality of both models are also expected to be the same [49, 50]. Accordingly, we have  $T_c(k_F, N_s) - T_c(k_F, N_s \rightarrow \infty) \sim N_s^{-1/(3\nu)} = L^{-1/\nu}$  with  $\nu = 2/3$  of the XY model [51, 52]. Here,  $\nu$  denotes the exponent of, for example, the correlation length, as  $\sim (T - T_c)^{-\nu}$ . Note that in comparison, a mean-field approximation such as Ginzburg-Landau theory gives  $\nu = 1/2$  [53]. With the linear  $N_s^{-1/2}$  dependence, we

find the best fits to the data for  $T_c$  at LO to be

$$\begin{aligned} T_c(k_F = 15 \text{ MeV}, N_s) &= 0.039(14) N_s^{-1/2} + 0.00700(94), \\ T_c(k_F = 30 \text{ MeV}, N_s) &= 0.1839(11) N_s^{-1/2} + 0.03420(11), \\ T_c(k_F = 60 \text{ MeV}, N_s) &= 0.6069(64) N_s^{-1/2} + 0.15770(30), \end{aligned} \quad (38)$$

which are shown in Fig. 8, and at NLO,

$$\begin{aligned} T_c(k_F = 60 \text{ MeV}, N_s) &= 0.88(19) N_s^{-1/2} + 0.146(13), \\ T_c(k_F = 90 \text{ MeV}, N_s) &= 1.14(33) N_s^{-1/2} + 0.388(22), \\ T_c(k_F = 120 \text{ MeV}, N_s) &= 1.67(63) N_s^{-1/2} + 0.687(37), \end{aligned} \quad (39)$$

which are shown in Fig. 9. The last constant in each best fit in Eqs. (38) and (39) is  $T_c$  at the thermodynamic limit,  $T_c(k_F, N_s \rightarrow \infty)$ .

While  $T^*$  is not at criticality, we find the finite-size scaling for  $T^*$  to be similar to that of  $T_c$ . For example, the data of  $T^*(N_s)$  yield the best-fit scaling power  $\sim N_s^{-0.507 \pm 0.007}$  with the jackknife method (for  $T_c$ ,  $\sim N_s^{-0.53 \pm 0.03}$ ). We thus apply the same linear  $N_s^{-1/2}$  dependence to  $T^*$  as that for  $T_c$ . The best fits for  $T^*$  at LO are found to be

$$\begin{aligned} T^*(k_F = 15 \text{ MeV}, N_s) &= 0.1400(24) N_s^{-1/2} + 0.00707(24), \\ T^*(k_F = 30 \text{ MeV}, N_s) &= 0.448(54) N_s^{-1/2} + 0.0463(23), \\ T^*(k_F = 60 \text{ MeV}, N_s) &= 1.45(15) N_s^{-1/2} + 0.2618(99), \end{aligned} \quad (40)$$

and at NLO,

$$\begin{aligned} T^*(k_F = 60 \text{ MeV}, N_s) &= 1.890(59) N_s^{-1/2} + 0.2575(35), \\ T^*(k_F = 90 \text{ MeV}, N_s) &= 3.583(60) N_s^{-1/2} + 0.5876(61), \\ T^*(k_F = 120 \text{ MeV}, N_s) &= 3.70(12) N_s^{-1/2} + 1.4320(69), \end{aligned} \quad (41)$$

where the last constant in each equation gives  $T^*$  at the thermodynamic limit.

As to the continuum limit, in Fig. 10 we show the  $n$  dependence of  $T_c$  and  $T^*$  at LO for  $N_s = 6^3$  at  $k_F = 60$  MeV. The data with statistical uncertainties are shown by solid circles for  $n = 1/16, 1/8, 3/16, 1/4, 3/8$ , and  $1/2$ . The exponent fit of  $T_c$  ( $T^*$ ) shows  $T_c \sim n^{0.31 \pm 0.12}$  ( $T^* \sim n^{0.43 \pm 0.10}$ ). As observed for the similar limit of  $T_c$  [42], they appear to be best fit by a linear  $n^{1/3}$  dependence,

$$T_c(n, N_s = 6^3)/\epsilon_F = -0.165(23) n^{1/3} + 0.209(12), \quad (42)$$

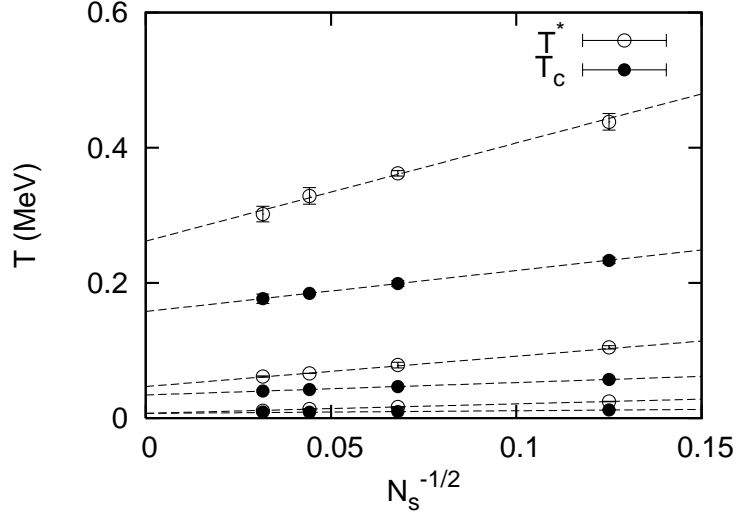


FIG. 8: Finite-size scaling of the critical temperature  $T_c$  and the pairing temperature scale  $T^*$ . The Monte Carlo data for  $T_c$  and  $T^*$  with  $n = 1/4$  at LO are shown for  $k_F = 15, 30$ , and  $60$  MeV from bottom to top. The dotted lines are the best fits of Eqs. (38) and (40).

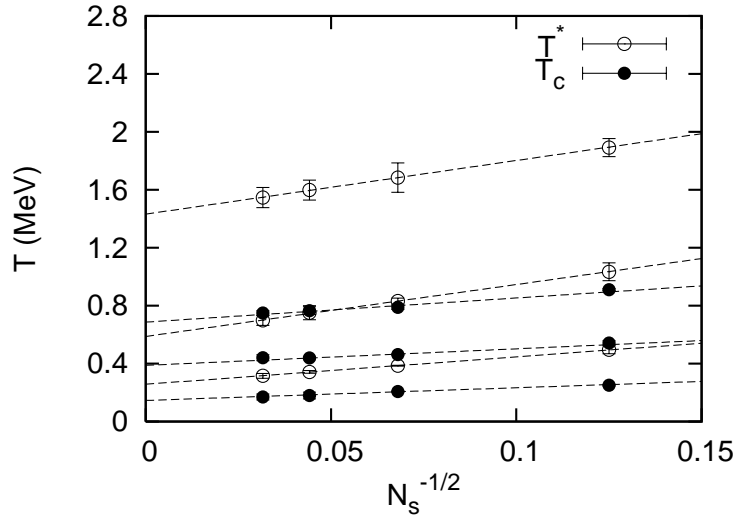


FIG. 9: Same as Fig. 8, for  $k_F = 60, 90$ , and  $120$  MeV, from bottom to top. The dotted lines are the best fits of Eqs. (39) and (41).

and

$$T^*(n, N_s = 6^3)/\epsilon_F = -0.286(20) n^{1/3} + 0.367(12). \quad (43)$$

Note that the continuum limits of  $T_c$  and  $T^*$  in Eqs. (42) and (43) are consistent with



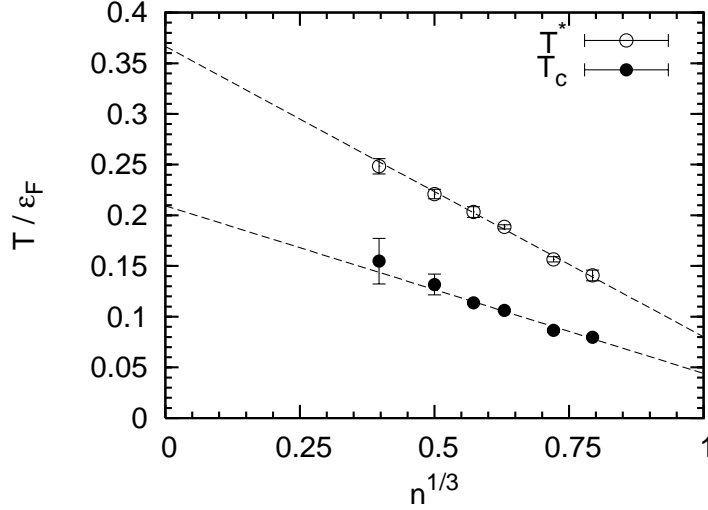


FIG. 10:  $n$  dependence of the critical temperature  $T_c$  and pairing temperature scale  $T^*$  at LO in the unit of the Fermi energy  $\epsilon_F$  for  $N_s = 6^3$  at  $k_F = 60$  MeV. The lines are the best fits to the  $T_c$  and  $T^*$  data, Eqs. (42) and (43), respectively.

those determined by the exponent fits using the jackknife method within the statistical uncertainties [ $T_c = 0.223(41)$  and  $T^* = 0.328(34)$ ]. Contrary to the case of  $\Delta$ , the  $n$  dependence of  $T_c$  and  $T^*$  is rather strong. Equations (42) and (43) provide the needed ratios  $R_{T_c}$  and  $R_{T^*}$ , which are used to obtain  $T_c$  and  $T^*$  at the thermodynamic and continuum limits, as in the case of  $\Delta$ .

### C. Dependence of the continuum limit on $N_s$ and $k_F$

The extrapolation to  $n \rightarrow 0$  depends generally on  $N_s$  and  $k_F$ , but the dependence is expected to be weak because of the separation of local (ultraviolet) and global (infrared) properties for a sufficiently large  $N_s$ .

For the  $N_s$  dependence, we calculate, using the lattice sizes of  $N_s = 4^3$  and  $8^3$ , the ratios between  $n \rightarrow 0$  and  $n = 0.25$ :  $R_\Delta$ ,  $R_{T_c}$ , and  $R_{T^*}$ , both at LO and NLO. As summarized in Table II, each ratio at  $k_F = 60$  MeV is consistent within the statistical uncertainties for  $N_s = 4^3$ ,  $6^3$ , and  $8^3$  both at LO and NLO. Note that the second row for  $N_s = 6^3$  is obtained using data at  $n = 1/16, 1/8, 3/16, 1/4, 3/16$ , and  $1/2$ , while the other rows use data at  $n = 1/16, 1/4$ , and  $1/2$ .

Table III also confirms the weak dependence on  $k_F$ . Note that the third row uses data for  $n = 1/16, 1/8, 3/16, 1/4, 3/8$ , and  $1/2$ , while the other rows use data at  $n = 1/16, 1/4$ , and  $1/2$ .

TABLE II: Dependence of the continuum limit on  $N_s$ .

	$k_F$ (MeV)	$N_s$	$R_\Delta$	$R_{T_c}$	$R_{T^*}$
LO	60	$4^3$	1.14(17)	2.10(15)	1.9(2)
LO	60	$6^3$	1.07(5)	1.96(13)	1.94(9)
LO	60	$8^3$	1.12(8)	1.86(10)	2.0(1)
NLO	60	$4^3$	1.08(6)	2.08(8)	2.1(2)
NLO	60	$6^3$	1.04(5)	2.05(7)	2.1(1)
NLO	60	$8^3$	1.05(4)	2.08(37)	2.0(1)

TABLE III: Dependence of the continuum limit on  $k_F$ .

	$k_F$ (MeV)	$N_s$	$R_\Delta$	$R_{T_c}$	$R_{T^*}$
LO	15	$6^3$	1.09(3)	1.96(9)	2.4(9)
LO	30	$6^3$	1.08(8)	1.98(6)	2.4(4)
LO	60	$6^3$	1.07(5)	1.96(13)	1.94(9)
NLO	60	$6^3$	1.04(5)	2.05(7)	2.1(1)
NLO	90	$6^3$	1.11(10)	2.12(20)	2.0(1)
NLO	120	$6^3$	1.04(2)	2.00(36)	2.0(3)

## V. MATCHING LO AND NLO RESULTS

Figures 11 and 12 display the LO and NLO  $\Delta$ 's as a function of  $k_F$  and illustrate their matching in the region of  $k_F = 0.15\text{-}0.30 \text{ fm}^{-1}$ : the  $\Delta$  shown in Fig. 11 is the result of the elaborate calculation described in Secs. III and IV, while the  $\Delta$  shown in Fig. 12 is the result of a simpler calculation for  $4^3$  lattices with  $n = 1/4$ , including  $\Delta$  at the density of

$k_F = 0.22805$ . The density dependences of the  $\Delta$ 's are quite close to each other in the two figures, demonstrating that a smooth transition from the LO  $\Delta$  to the NLO  $\Delta$  occurs in the density region of  $k_F = 0.15$ - $0.30 \text{ fm}^{-1}$ . Accordingly, we take the LO  $\Delta$  for  $k_F = 0.1520 \text{ fm}^{-1}$  and the NLO  $\Delta$  for  $k_F = 0.3041 \text{ fm}^{-1}$ , as the final values.

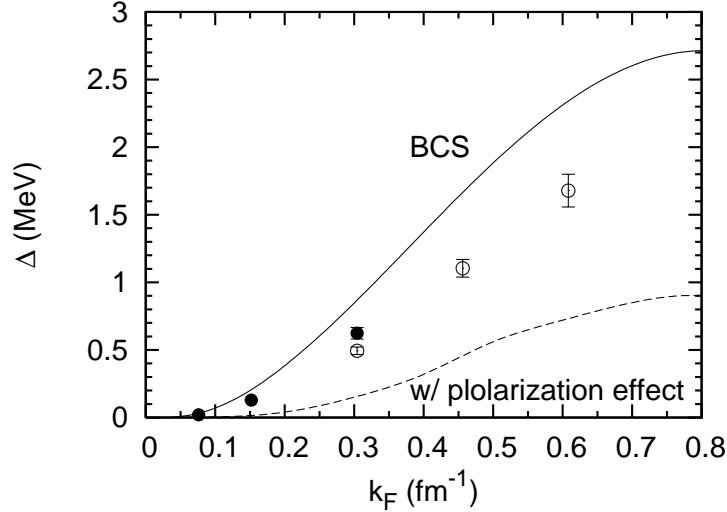


FIG. 11:  $^1S_0$  pairing gap,  $\Delta$ , in the thermodynamic and continuum limits, resulting from the LO (solid circles) and NLO (open circles) calculations. The neutron density is denoted in terms of the Fermi momentum  $k_F$ . The BCS calculation of Ref. [54] (solid curve) and a higher order calculation including polarization effects of Ref. [55] (dashed curve) are also shown for comparison. For a more detailed comparison, see Fig. 17 in Sec. VII B.

Figure 13 shows that also for  $T_c$  and  $T^*$ , smooth transitions take place between the LO and NLO values in the same density region as for  $\Delta$ . We thus also take  $T_c$  and  $T^*$  at  $k_F = 0.1520 \text{ fm}^{-1}$  as the LO and  $T_c$  and  $T^*$  at  $k_F = 0.3041 \text{ fm}^{-1}$  as the NLO. Note that the difference between the LO and NLO values of  $T_c$  and  $T^*$  in Fig. 13 is much smaller than that in the case of  $\Delta$ .

## VI. RESULTS

### A. Pairing gap $\Delta$

Table IV lists our final values of  $\Delta$  in the thermodynamic and continuum limits for low-density neutron matter. Table IV includes the ratio of  $\Delta$  and the corresponding BCS

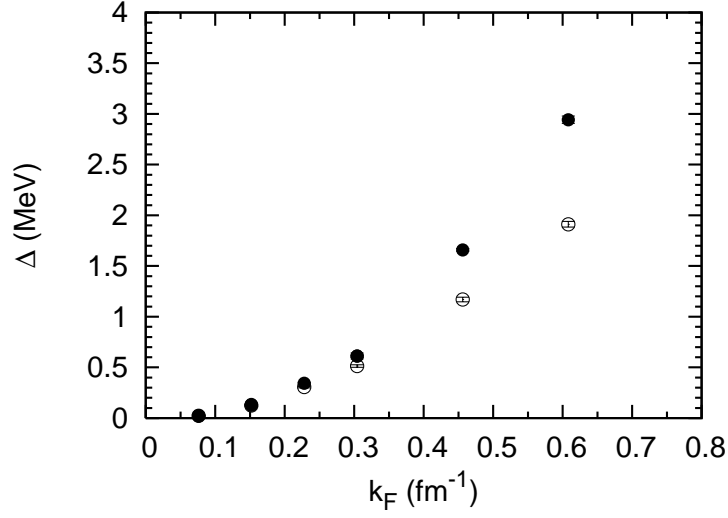


FIG. 12:  $^1S_0$  pairing gap,  $\Delta$ , for  $N_s = 4^3$  and  $n = 1/4$ , resulting from the LO (solid circles) and NLO (open circles) calculations. The neutron density is denoted in terms of the Fermi momentum  $k_F$ .

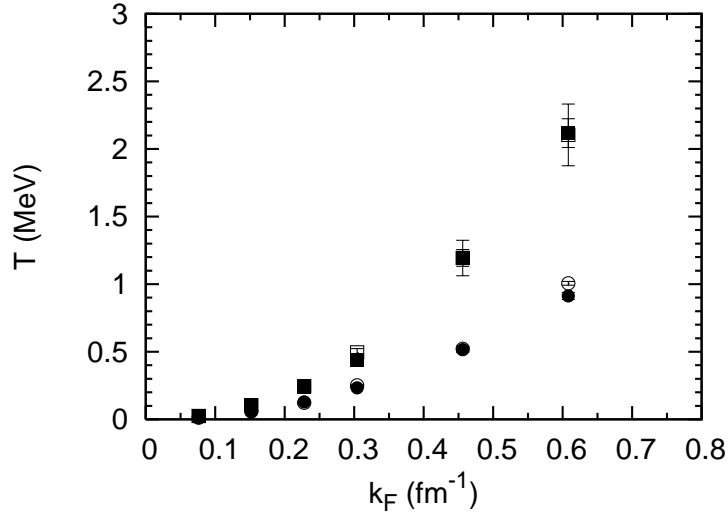


FIG. 13: Critical temperature  $T_c$  (circles) and the pairing temperature scale  $T^*$  (squares) by the LO (solid symbols) and NLO (open symbols) calculations for  $N_s = 4^3$  and  $n = 1/4$ , shown as a function of the neutron matter density (represented by the Fermi momentum  $k_F$ ). The error bars are statistical uncertainties only.

TABLE IV: Our final values of the  $^1S_0$  pairing gap  $\Delta$  in the thermodynamic and continuum limits, and the ratio of  $\Delta$  and the BCS value  $\Delta_{\text{BCS}}$ . Uncertainties are statistical only.

$k_F$ (MeV)	$\rho$ ( $\rho_0$ )	$\Delta$ (MeV)	$\Delta/\Delta_{\text{BCS}}$
15	$9 \times 10^{-5}$	0.021(1)	0.69(3)
30	$7 \times 10^{-4}$	0.13(1)	0.67(4)
60	$6 \times 10^{-3}$	0.49(3)	0.56(5)
90	$2 \times 10^{-2}$	1.10(7)	0.68(4)
120	$5 \times 10^{-2}$	1.7(1)	0.74(4)

pairing gap,  $\Delta_{\text{BCS}}$ . Here, the  $\Delta_{\text{BCS}}$ 's are taken from those tabulated in Ref. [54] as the representative BCS values. As noted in Sec. VII B, there are only quite small differences among the  $\Delta_{\text{BCS}}$ 's calculated by the CD-Bonn, Nijmegen I, Nijmegen II, and Argonne V18  $NN$  potentials [10, 11].

It is difficult to assess the systematic uncertainties involved in our calculation. In view of the probable uncertainties involved in taking the thermodynamic limit and especially the continuum limit, however, it would be fair to state that our calculation yields  $\Delta$  to be approximately 30% less than the BCS values, perhaps with an additional systematic uncertainty of about  $\pm 10\%$ . We thus consider finer variations of  $\Delta$  inconclusive. For example, a close examination of Table IV shows that the  $\Delta/\Delta_{\text{BCS}}$  ratio dips at around  $k_F = 60$  MeV. But this would require further study.

## B. Phase diagram of low-Density neutron matter

Table V lists our final values of  $T_c$  and  $T^*$  in the thermodynamic and continuum limits. It also shows their ratios and the ratios with the  $\Delta$  of Table IV. In Table V, we observe that  $T^*$  approaches  $T_c$  as the density decreases. That is, the pseudogap state (see below) diminishes as the density decreases. Furthermore, as the density decreases, the  $\Delta/T_c$  ratio approaches the BCS value of about 1.76 [56], while  $\Delta$  and  $T_c$  themselves remain different from the BCS values.

$T_c$  and  $T^*$  in Table V provide the temperature-density phase diagram as shown in Fig. 14.

The figure illustrates the thermodynamic properties of low-density neutron matter. For example, at a fixed density  $k_F$ , as the temperature goes down from the normal phase, the pairing is gradually enhanced, forming the pseudogap phase [49] around and below  $T^*$ . As the temperature goes down farther, the pairing gets stronger and eventually forms a long-range ordering at  $T_c$ , thereby generating the second-order phase transition to the superfluid phase. Note that the transition between the pseudogap phase and the normal phase is smooth. We must also note that the definition of  $T^*$  is somewhat subjective.

TABLE V: Our final values of  $T_c$  and  $T^*$ , and the relative magnitudes among them and  $\Delta$  in Table IV.

$k_F$ (MeV)	$T_c$ (MeV)	$T^*$ (MeV)	$\Delta/T_c$	$\Delta/T^*$	$T_c/T^*$
15	0.014(3)	0.014(1)	1.5(4)	1.5(2)	0.99(28)
30	0.067(5)	0.091(9)	1.6(2)	1.4(2)	0.74(12)
60	0.29(5)	0.45(5)	1.7(4)	0.99(11)	0.57(12)
90	0.76(9)	1.1(1)	1.5(3)	0.97(11)	0.67(12)
120	1.4(2)	2.8(1)	1.2(2)	0.60(7)	0.49(8)

## VII. DISCUSSIONS

### A. Nature of low-density neutron matter: BCS-BEC crossover

To understand the nature of low-density neutron matter, we examine the dependence of  $T_c$  on the parameter  $c_0$  by applying the LO calculation, since the physics throughout our low-density region is largely dictated by  $c_0$ . Figure 15 illustrates the dependence in comparison to  $T_c$  in the weak-coupling (BCS) and strong-coupling (BEC) limits,

$$T_c(\text{BCS}) = \frac{2e^\gamma}{\pi} \sqrt{(36t^2 - \mu^2)} \exp\left(-\frac{a^3}{D_0(\mu)|c_0|}\right), \quad (44)$$

$$T_c(\text{BEC}) = 2 \left( \frac{2\pi^2 n}{\Gamma(3/2)\zeta(3/2)} \right)^{2/3} \frac{a^3 t^2}{|c_0|},$$

respectively [48]. Here,  $\gamma$  is Euler's constant and  $D_0(\mu)$  is the density of states. In our low-density neutron matter,  $|c_0|/(a^3 t)$  is 5-7, and corresponds to the middle region in Fig. 15.

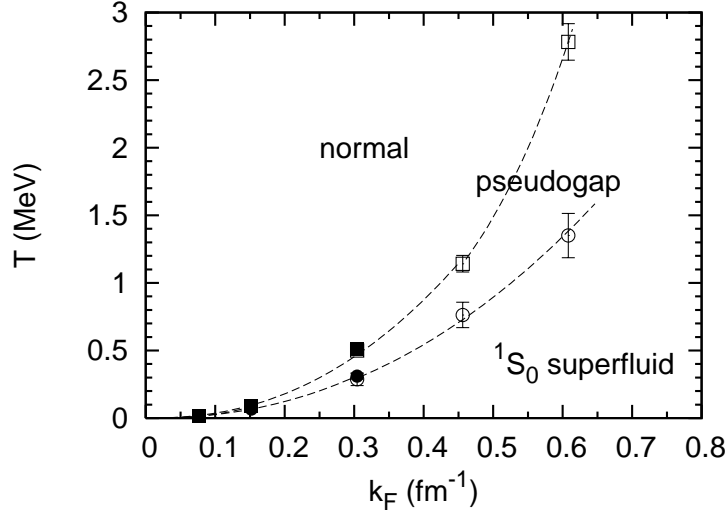


FIG. 14:  $^1S_0$  phase diagram of low-density neutron matter. The solid and open symbols with statistical uncertainties show the LO and NLO results, respectively. The dotted curves for  $T_c$  and  $T^*$  are drawn by extrapolation. Neutron matter is in the superfluid phase below the critical temperature  $T_c$  of the second-order phase transition. Above  $T_c$ , neutron matter is in the pseudogap phase [49], in which pairing remains locally without forming long-range order, and undergoes a smooth transition from the pseudogap phase to the normal phase around  $T^*$ , as pairing gets much less.

The figure clearly shows that *the thermal property of low-density neutron matter is not in a state of BCS, but of BCS-BEC crossover*. Though not discussed here, the  $c_0$  dependence of  $T^*$  also verifies this point [47, 48].

The preceding point is perhaps better clarified by the  $c_0$  dependence of the chemical potential  $\mu$ .  $\mu$  is positive in the weak-coupling BCS region and becomes negative in the strong-coupling BEC region by exhibiting a bosonic nature. Figure 16 illustrates the  $c_0$  dependence of  $\mu$  in the LO calculation.  $\mu$  decreases as  $c_0$  increases, and it takes a relatively small, positive value in the region of our low-density neutron matter. The small positive value is in accord with the neutron matter being close but not (yet) in the BEC region and indeed confirms the simple characterization of the crossover, a negative and small (in magnitude) value of  $1/(k_F a_0)$  [28], as noted in Sec. I.

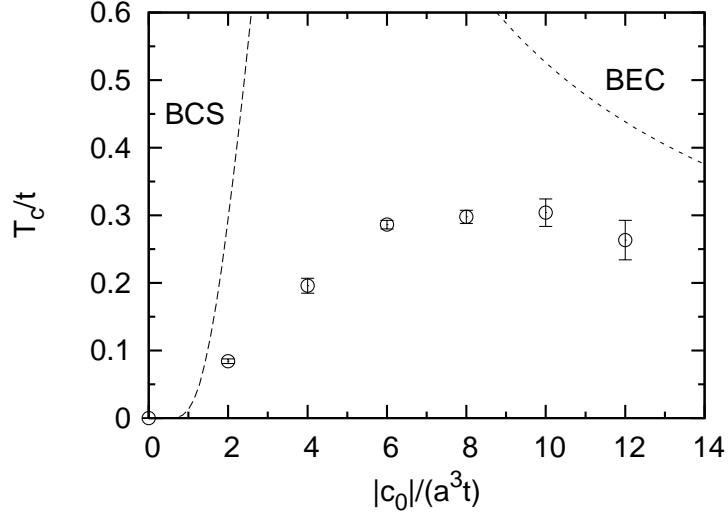


FIG. 15: EFT parameter ( $c_0$ ) dependence of the critical temperature  $T_c$ . For easier comparison,  $T_c$  and  $c_0$  are expressed as dimensionless by use of the spatial lattice spacing  $a$  and the hopping parameter  $t$ . The open circles are shown for  $N_s = 6^3$  at the quarter-filling ( $n = 0.5$ ). The dashed curves are  $T_c/t$  at the BCS and BEC limits of Eq. (44).

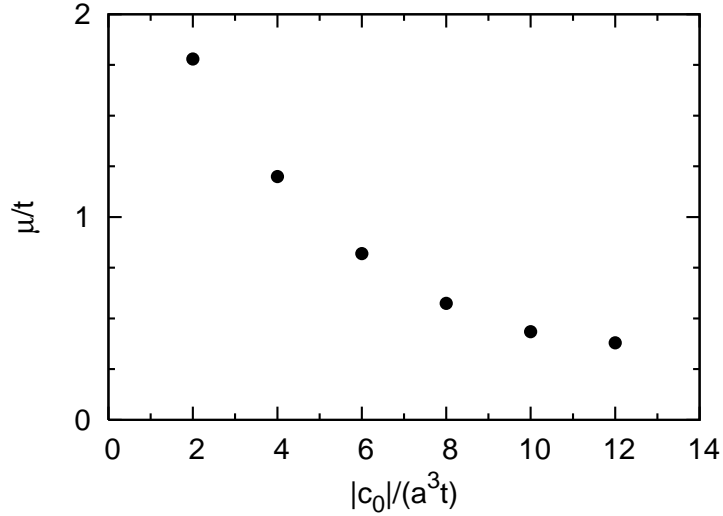


FIG. 16: Chemical potential  $\mu$  as a function of the interaction strength  $c_0$  in a dimensionless unit, with the spatial lattice spacing  $a$  and the hopping amplitude  $t$ . The calculation is of the LO for  $N_s = 6^3$  and  $n = 0.5$ .



## B. Pairing gap $\Delta$

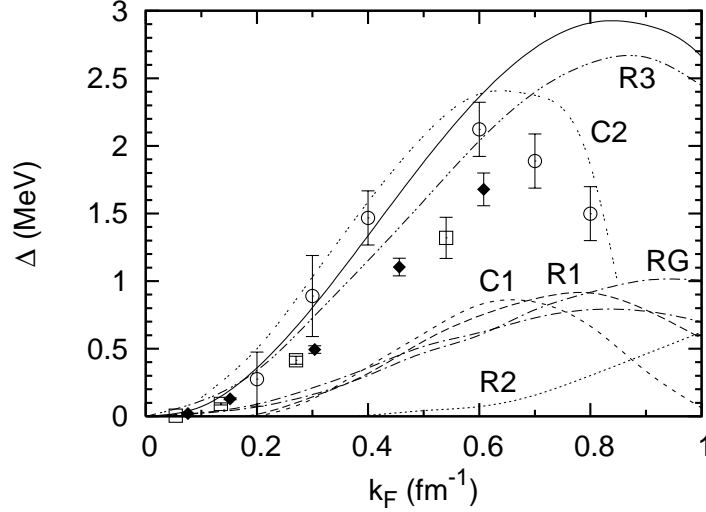


FIG. 17: Comparison of our Monte Carlo  $\Delta$  to other calculations as a function of the neutron matter density (represented by the Fermi momentum  $k_F$ ). The solid diamonds show our results, with statistical uncertainties. The other calculations consist of three types: quantum Monte Carlo (symbols with statistical uncertainties), BCS (solid curve), and BCS with higher-order effects (R's, C's, and RG; shown by dotted and dashed curves). See text for the description of each calculation shown.

Figure 17 illustrates the density dependence of various  $\Delta$ 's reported in the literature.  $\Delta$ 's in the figure consist of those obtained by three types of calculations: (1) BCS (shown by a solid curve), (2) BCS or similar approximations, with higher order effects (dotted and dashed curves), and (3) quantum Monte Carlo (shown with error bar symbols).

(1) Below  $k_F \approx 0.7 \text{ fm}^{-1}$ , there are few recognizable differences [10, 11] among  $\Delta_{\text{BCS}}$ 's calculated by various conventional  $NN$  potentials: Argonne  $v_{18}$  [57], Nijmegen [58], and CD Bonn [59]. Accordingly,  $\Delta_{\text{BCS}}$ 's are represented by a single (solid) curve in Fig. 17.

(2) Figure 17 includes  $\Delta$ 's by the calculations beyond BCS. Calculations in the random phase approximation (RPA) with polarization effects are by Wambach *et al.* [55] (denoted as R1), by Schulze *et al.* [60] (R2), and by Cao *et al.* [61] (R3). Calculations using correlated-basis functions are by Chen *et al.* [62] (C1) and by Fabrocini *et al.* [16] (C2). A calculation based on a renormalization group approach is by Schwenk *et al.* [63] (RG). The curves for

these  $\Delta$ 's are taken from similar figures in the recent literature: Figs. 1 and 2 of Ref. [17] and Fig. 4 of Ref. [14]. In addition, though not shown, an extrapolation from finite nuclei results obtained by Hartree-Fock-Bogoliubov calculations also gives  $\Delta$  close to the  $\Delta_{\text{BCS}}$  for  $k_F \lesssim 0.5 \text{ fm}^{-1}$  [64]. We see that these  $\Delta$ 's differ appreciably among each other, though recent works tend to give the values closer to the BCS  $\Delta$ .

(3) Two types of quantum Monte Carlo calculations have been reported based on the GFMC [13, 14] and AFDMC [16, 17] methods. The two methods are applied for a fixed number of neutrons using the conventional  $NN$  potentials (or some model potentials), while our work is based on a grand canonical ensemble formulation. Figure 17 shows the most recent results of the GFMC [14] (open squares), the AFDMC [17] (open circles), and ours (taken from Table IV and shown by solid diamonds).

In the figure, we see that all quantum Monte Carlo calculations are, overall, close to the  $\Delta_{\text{BCS}}$ . The AFDMC  $\Delta$  is quite close to the  $\Delta_{\text{BCS}}$  in the density region examined in this work, while the GFMC  $\Delta$  is smaller than the  $\Delta_{\text{BCS}}$  and is similar to (even slightly lower than) our  $\Delta$ . Note that above  $k_F \approx 0.6 \text{ fm}^{-1}$ , the AFDMC  $\Delta$  becomes quickly smaller than the  $\Delta_{\text{BCS}}$  as the density increases.

It is difficult to assess the three quantum Monte Carlo calculations by comparing them because the intermediate steps of the calculations are all different. Here, however, we point out a possible issue closely tied to their basic formulations and setups: stemming from the neutron numbers being fixed, the GFMC and AFDMC  $\Delta$ 's are calculated using the odd-even staggering (or the second-order finite difference) of the energy per neutron,

$$\Delta(\text{odd } N) = E(N) - \frac{1}{2} [E(N-1) + E(N+1)], \quad (45)$$

where  $N$  is the number of neutrons. As described in Sec. III, our  $\Delta$ 's are calculated directly from the spin pair-pair correlation functions. By physical arguments, the two ways of calculating  $\Delta$  are expected to be the same for a large  $N$ , but we are not aware of a rigorous proof for this expectation. Since it has been a common practice to apply Eq. (45) for the extraction of  $\Delta$  from finite nuclei [1, 27], closer examination of this issue would be desirable, as exemplified in Ref. [64].

As noted above, it is desirable to apply Eq. (45) for a large  $N$ . The large values up to  $N = 92$  are used in the GFMC calculation [14], while up to  $N = 68$  in the AFDMC [17]. Both  $N$ 's are perhaps large enough to provide reliable information for  $N \rightarrow \infty$ . While it

might be caused by the different ways the nuclear potentials are applied in the two methods, the noticeable difference between the GFMC and AFDMC  $\Delta$ 's is puzzling to us.

### C. Further improvement of the present work

We note here the aspects of this work that we would like to improve.

(1) The largest lattice size we have used is  $N_s = 10^3$ , but larger lattices would be desirable for reliably reaching the thermodynamic limit. For this, we would like to study more closely the use of the hybrid Monte Carlo (HMC) method. As the commonly used method in lattice QCD calculations [38], the HMC is expected to reduce the computation time from  $\sim (N_s N_t)^2$  or  $(N_s N_t)^3$  (for the DQMC) to  $\sim (N_s N_t)^{5/4}$ . Our trial application of the HMC (following Ref. [65]) in our problem has shown a strong dependence on the HMC parameters, such as the size and number of molecular dynamics steps and has brought about a difficult compromise between the computation time and the systematic error. We suspect that the difficulty stems from badly conditioned fermion matrices and also from our (effectively) strong interaction. We would like to resolve this issue and find a practical procedure for optimizing the HMC calculation for this problem.

(2) Because of lack of time, we have examined the continuum limit by applying the case of  $N_s = 6^3$  to all  $N_s$ 's that we computed. The possible  $N_s$  dependence is a potentially important source of the systematic error, and we would like to clarify this issue.

(3) The matching of the LO and NLO calculations indicates that our  $\Delta$  deviates from the  $\Delta_{\text{BCS}}$  more appreciably in the matching density region,  $k_F \approx 0.15\text{-}0.3 \text{ fm}^{-1}$ . It is difficult to establish the deviation by using the present statistics. We would like to examine this density region more closely to determine whether such a fine structure of the density dependence of  $\Delta$  exists.

## VIII. SUMMARY

In conclusion, we have investigated thermal properties of low-density neutron matter by the determinantal quantum Monte Carlo lattice calculations with the single- and two-parameter pionless EFT  $NN$  potential. The  $^1S_0$  pairing gap at  $T \approx 0$ , the critical temperature of normal-to-superfluid phase transition, and the pairing temperature scale have

been determined directly from the correlation functions and have provided the temperature-density phase diagram for the density of  $(10^{-4}\text{-}10^{-1})\rho_0$ . The thermodynamic limit was taken, and the continuum limit was examined in the determination. The pairing gap was found to be approximately 30% less than the BCS value. The physics of neutron matter in this density region has clearly been identified as a BCS-BEC crossover.

## ACKNOWLEDGMENTS

We thank U. van Kolck for his continuing support for our project by clarifying various aspects and issues on EFT, especially those associated with the power counting rules and regularization procedure. We acknowledge H. M. Müller for allowing our use and modification of his code, D. Lee for his useful comments after reading the initial version of the manuscript, and K.-F. Liu and T. Onogi for their instructive comments on our lattice calculations. The calculations were carried out on Seaborg, Bassi, and Franklin at the National Energy Research Scientific Computing Center, which is supported by the Office of Science of the U.S. Department of Energy under Contract No. DE-AC03-76SF00098, and at Titech Grid and TSUBAME, Tokyo Institute of Technology, Japan. The major part of this work was carried out at Kellogg Radiation Laboratory, Caltech. We thank R. McKeown for his generous hospitality over the years. A part of this work was also performed at the Yukawa Institute for Theoretical Physics (YITP), Kyoto University. R. S. is grateful for the warm hospitality received at the YITP. This work is supported by the U.S. Department of Energy under Grant No. DE-FG02-87ER40347 at CSUN.

## APPENDIX A: DETERMINATION OF THE EFT POTENTIAL PARAMETERS

### $c_0(\Lambda)$ AND $c_2(\Lambda)$

The EFT potential parameters,  $c_0(\Lambda)$  and  $c_2(\Lambda)$ , are determined from the observables for an appropriately chosen value of  $\Lambda$ . As the observables, we choose the scattering length  $a_0$  and the effective range  $r_0$  in the effective range expansion of Eq. (6) with  $\Lambda = \pi/a$  in our lattice calculation (where  $a$  is the lattice spacing).

$\Lambda$  is needed in the determination of  $c_0(\Lambda)$  and  $c_2(\Lambda)$  so as to regularize loop contributions, which otherwise diverge. With the regularization, the Schrödinger equation is solved, and  $a_0$  and  $r_0$  are expressed in terms of  $c_0(\Lambda)$  and  $c_2(\Lambda)$  algebraically [37, 66]. The direct use of the algebraic expressions, however, amounts to a mere phenomenological fit. As an application of EFT, we must ensure that EFT counting rules are properly applied: because our EFT Lagrangian is truncated at  $p^2/\mathcal{Q}^2$ , we must be consistent with the truncation in the determination of  $c_0$  and  $c_2$ . That is,  $c_2(\Lambda)$  must be treated perturbatively by neglecting the  $\mathcal{O}([c_2(\Lambda)]^2)$ -order contributions. We then obtain [37]

$$\begin{aligned}\frac{M}{4\pi} \frac{1}{a_0} &= \left[ \frac{1}{c_0(\Lambda)} + \frac{M}{2\pi^2} L_1 \right] + \frac{M}{\pi^2} L_3 \frac{c_2(\Lambda)}{c_0(\Lambda)}, \\ \frac{M}{16\pi} r_0 &= \frac{c_2(\Lambda)}{c_0^2(\Lambda)} - \frac{M}{4\pi^2} \frac{1}{\Lambda} R(0),\end{aligned}\tag{A1}$$

where  $L_1 = \theta_1 \Lambda$  and  $L_3 = \theta_3 \Lambda^3$ . The numerical values of  $\theta_1, \theta_3$ , and  $R(0)$  for large lattices are given in Ref. [37]. The inversion of Eq. (A1) is, again by treating  $c_2(\Lambda)$  perturbatively,

$$\begin{aligned}c_0(\Lambda) &= c_0^{(0)}(\Lambda) \left\{ 1 + \frac{r_0}{\pi} \left( \frac{M}{4\pi} \right)^2 L_3 \eta [c_0^{(0)}(\Lambda)]^2 \right\} \equiv c_0^{(0)}(\Lambda) + \Delta c_0(\Lambda), \\ c_2(\Lambda) &= \frac{M r_0}{16\pi} \eta [c_0^{(0)}(\Lambda)]^2,\end{aligned}\tag{A2}$$

where  $\eta = 1 + 4R(0)/(\pi r_0 \Lambda)$ , and the leading-order  $c_0(\Lambda)$ ,  $c_0^{(0)}(\Lambda)$ , is given by

$$c_0^{(0)}(\Lambda) = \frac{4\pi}{M} \left( \frac{1}{a_0} - \frac{2}{\pi} L_1 \right)^{-1}.\tag{A3}$$

Equations (A1) and (A2) consistently include up to  $\mathcal{O}(p^2/\mathcal{Q}^2)$ ; their combined use is equivalent to solving the Schrödinger equation with the truncated potential of Eq. (A2) *by treating  $c_2(\Lambda)$  perturbatively*. That is, in this treatment, we obtain exactly the same  $a_0$  and  $r_0$  as those determined phenomenologically or obtained by solving the Schrödinger equation with no counting rule applied. Because of this, the phase shifts determined by

$a_0$  and  $r_0$  are also exactly the same as those determined by the LO and NLO potentials by consistently applying the EFT counting rule. The same EFT treatment should also be applied to calculations of many-nucleon systems, as we have done in this work. Note that upon the application of the EFT counting rule, consistency is the vital point, as is evident from the observation that  $r_0$  turns out to be negative for a certain range of  $\Lambda$  if this step is not properly applied [66].

For  $a_0$  and  $r_0$ , we have used the old values of  $-16.45$  fm and  $2.83$  fm, respectively [67, 68]. The most recent values are  $a_0 = -18.9 \pm 0.4$  fm and  $r_0 = 2.75 \pm 0.11$  fm as quoted in Ref. [36]. The discrepancy between the two  $a_0$  values is  $13 \pm 2$  % and not negligible, but its effects are expected to be much smaller.

As Eq. (A3) implies,  $c_0^{(0)}$  is dominated by the  $\Lambda$  contribution because  $c_0^{(0)}$  is close to the nontrivial fixed point in the renormalization group flow [30, 69], dictated by the large magnitude of  $a_0$ . Consequently,  $c_0$  and  $c_2$  are quite insensitive to the exact value of  $a_0$ . For example, at  $k_F = 60$  MeV, using the standard parameter set of Table I, the NLO  $c_0/(a^3 t)$  and  $c_2/(a^5 t)$  differ by 1.8% and 1.4%, respectively, between the old and the most recent values of  $a_0$  and  $r_0$ . The corresponding LO  $c_0/(a^3 t)$  differs by 1.4% between them.

Generally some  $\Lambda$  contributions must cancel in calculating observables, so that their values are independent of the regularization procedure. But the closeness to the fixed point suggests the cancellation to be effectively small in this case. Although repeating our entire calculations is quite time consuming and unrealistic at present, we have performed a limited, test LO calculation at  $k_F = 60$  MeV for  $N_s = 6^3$  and  $n = 1/4$ . We find  $\Delta$  differs by about 2%, in the same order of the statistical uncertainties of the Monte Carlo calculation:  $\Delta = 0.63(1)$  and  $= 0.64(3)$  MeV for  $a_0 = -16.45$  and  $= -18.9$  fm, respectively. This finding also confirms the following observation: in the accompanying paper [29], we report the determination of various quantities at the unitary limit ( $|a_0| \rightarrow \infty$  with  $r_0 = 0$ ) by making the extrapolation  $\eta \equiv 1/(a_0 k_F) \rightarrow 0$ . By taking the  $\eta$  variation to be an  $a_0$  variation, we find that the above discrepancy in  $\Delta$  is 2.2% for  $k_F = 60$  MeV and decreases as  $k_F$  gets larger and increases as  $k_F$  gets smaller.

## APPENDIX B: PHYSICAL SIZES OF A NEUTRON PAIR AND COMPUTATIONAL LATTICE

A measure of the size of an interacting neutron pair (a Cooper pair) in the superfluid state,  $\xi_{\text{cp}}$ , is [27]

$$\xi_{\text{cp}} = \frac{\hbar^2 k_F}{M\Delta}. \quad (\text{B1})$$

$\xi_{\text{cp}}$  must be smaller than the dimension of the cubic lattice, as a necessary condition for the simulation of the collective state (but clearly not a sufficient one). Table VI shows that  $\xi_{\text{cp}}$  is indeed much smaller than the dimension of the lattice  $aN_s^{1/3}$ , except for the marginal case of  $N_s = 4^3$ . Note that  $\xi_{\text{cp}}$  depends on  $a$  and  $L$  through the  $n$  dependence of  $\Delta$ . The  $a$  and  $N_s$  dependence of  $\xi_{\text{cp}}$  through  $\Delta$  is weak, as seen in Sec. IV A. In the table, we list  $\xi_{\text{cp}}$  for  $N_s = 4^3$  and  $n = 1/4$ , for simplicity.

TABLE VI: Physical sizes of a neutron pair and computational lattices.

$k_F$ (MeV)	$\xi_{\text{cp}}$ (fm)	$a$ (fm)	$aN_s^{1/3}$ ( $N_s = 4^3$ )	$aN_s^{1/3}$ ( $N_s = 6^3$ )	$aN_s^{1/3}$ ( $N_s = 8^3$ )	$aN_s^{1/3}$ ( $N_s = 10^3$ )
15	$1.3 \times 10^2$	25.64	102.6	153.8	205.1	256.4
30	47	12.82	51.3	76.9	102.6	128.2
45	28	8.55	34.2	51.3	68.4	85.5
60	21	6.41	25.7	38.5	51.3	64.1
90	11	4.27	17.1	25.6	34.2	42.7
120	8.6	3.21	12.8	19.2	25.6	32.1

## APPENDIX C: TECHNICAL DETAILS OF MONTE CARLO COMPUTATION

In this appendix, we discuss some technical details of the setup for the implementation of our lattice calculations.

## 1. Parameter values

The parameter set for lattice sizes is the following: the number of spatial lattice sites used are

$$N_s = 4^3, 6^3, 8^3, \text{ and } 10^3, \quad (\text{C1})$$

so as to extrapolate the data into the thermodynamic limit ( $N_s \rightarrow \infty$ ); the number of temporal lattice sites is

$$4 \leq N_t \leq 128, \quad (\text{C2})$$

where the discretization size of the temporal lattice is the same in Ref. [47] as

$$\Delta N_t = \frac{0.125}{t}. \quad (\text{C3})$$

The typical example of one production run is as follows. Because the method of grand canonical ensemble is used,  $\mu$  is fixed in each run. The thermal observable for the desired density  $\rho$  is interpolated from a few sets of the observables calculated at different  $\mu$ . About 1000-10000 samples are accumulated to obtain statistics with a precision of several percent.

## 2. Determinantal quantum Monte Carlo

### *a. Temporal lattice spacing*

To choose  $\Delta\beta$ , we need to know how the expectation values of thermal observables are affected by the choice. Figure 18 illustrates the dependence of  $\Delta\beta$  on the thermal observable  $C_\Delta$  in our DQMC calculation. The data have been taken with  $\mu/t = 0$  and  $N_s = 4^3$  at  $k_F = 30$  MeV. The figure is a typical example, and we have observed similar results with other thermal observables and parameter values.

From Fig. 18, we see that the expectation values of thermal observables are affected only a little for  $\Delta\beta \lesssim 0.2t$ , confirming that the choice employed in the previous DQMC calculation similar to ours [20] is indeed reasonable, and so we adopted this choice.

### *b. Prethermalization steps*

At the start of sampling, we generate the initial configuration of the auxiliary fields  $\chi$ . In our DQMC calculation, we use the hot start, in which a random (disordered) configuration



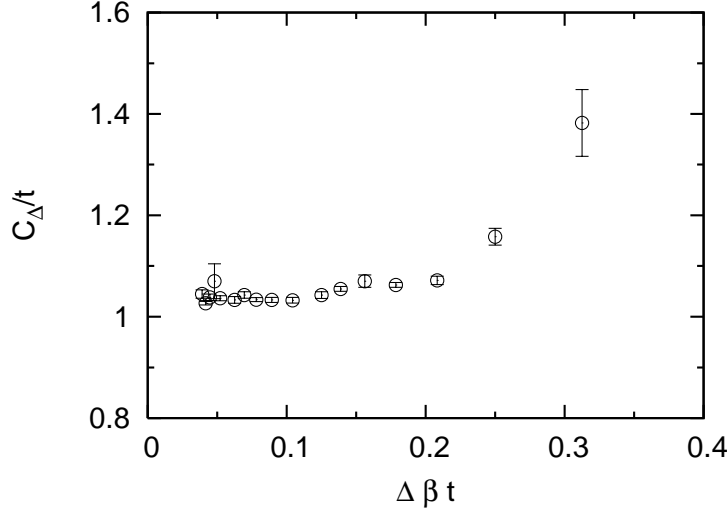


FIG. 18: Pair correlation function  $C_\Delta$  as a function of temporal lattice spacing  $\Delta\beta$ , with  $N_s = 4^3$  at  $k_F = 30$  MeV in the unit of hopping amplitude  $t$  in the DQMC calculation.

is used, instead of the cold start using a uniform (ordered) configuration. Following the start, we must take a sufficient number of prethermalization steps to obtain the equilibrium configurations, statistically independent from the initial configuration in the Markov chain.

Figure 19 illustrates the dependence of the sample number on the thermal observable  $C_\Delta$  in our DQMC calculation. The data have been taken with  $\mu/t = -1.83$  at  $N_s = 4^3$  and  $N_t = 12$ . The figure shows that the equilibrium starts to be reached after 100-150 samples. Similar results are observed with other observables and for other parameter values.

### *c. Thermalization steps and autocorrelations*

To ensure statistically independent configurations, we must take thermalization (decorrelation) steps between sample takings. We determine the number of the thermalization steps by monitoring the autocorrelation. The autocorrelation for  $k$  conservative samples of the observable  $O$ ,  $C_O(k)$ , is of the standard form

$$C_O(k) = \frac{\langle O_i O_{i+k} \rangle - \langle O_i \rangle^2}{\langle O_i^2 \rangle - \langle O_i \rangle^2} \quad (\text{C4})$$

where  $\langle \dots \rangle$  denotes the average over the random walk labeled with  $i$ , for example,

$$\langle O_i O_{i+k} \rangle \equiv \frac{1}{N-1} \sum_{i=1}^{N-k} O(X_i) O(X_{i+k}). \quad (\text{C5})$$

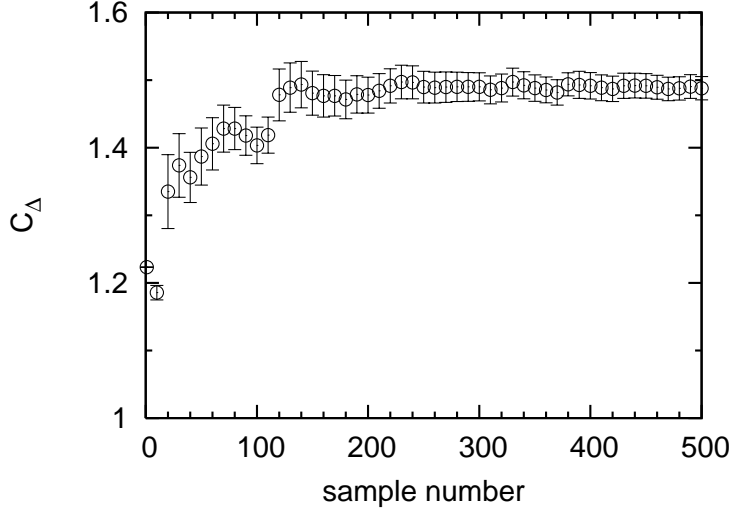


FIG. 19: The pair correlation function  $C_\Delta$  as a function of the sample number at  $N_s = 4^3$  and  $N_t = 12$  in the unit of hopping amplitude  $t$  in our DQMC calculation.

The condition of no correlation is  $C_O \sim 0$ , but in practical terms  $C_O \lesssim 0.1$  is recommended [70], and thus we ensure  $C_O$  to be less than 10% .

A typical case of the autocorrelations for some observables is shown in Fig. 20 with the parameter set ( $N_s = 4^3$ ,  $N_t = 12$ , and  $k_F = 30$  MeV). The autocorrelations are seen to be less than 0.1 for more than ten thermalization steps between samples.

### 3. Systematic error of the DQMC

Here, we discuss the systematic uncertainties of the DQMC besides the statistical ones due to data sampling. After ensuring the independence between samples by keeping the autocorrelations of thermal observables small enough as described in Appendix A 2, the systematic error of the DQMC on observables solely comes from the size of the discretization of the time slice  $\Delta\beta$ , which is related to the inverse of temperature  $\beta \equiv N_t \Delta\beta$ .

For confirming the consistency of our DQMC calculation with others, we compare  $T_c/t$  with that in Refs. [47, 48] over the various interaction strengths  $c_0/(a^3t)$  at fixed temporal lattice spacing  $\Delta\beta = 0.125/t$ , which has been commonly used in the condensed-matter physics. For estimating the systematic errors caused by finite  $\Delta\beta$ , the  $\Delta\beta$  dependence of  $\Delta$ ,  $T_c$ , and  $T^*$  have also been further examined.

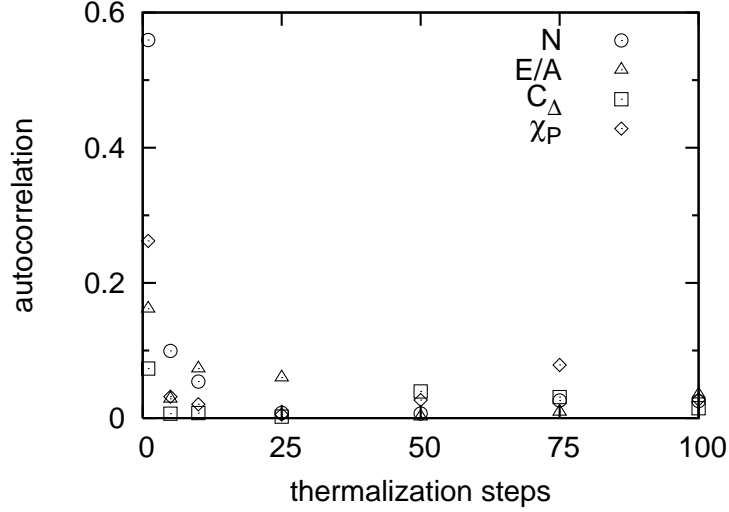


FIG. 20: Autocorrelation as a function of thermalization steps between samples taken with the number of spatial lattice sites  $N_s = 4^3$  and of temporal lattice sites  $N_t = 12$  at the Fermi momentum  $k_F = 30$  MeV in our DQMC calculation.

By these preliminary DQMC calculations, we can ensure the consistencies of DQMC calculations with those in other literature. The systematic uncertainties caused by our calculations with finite  $\Delta\beta$  amount to around 10%.

*a. Comparison of  $T_c(c_0/(a^3t))$  with other work*

First we ensure that our DQMC calculation at finite  $\Delta\beta$  is consistent with other literature. Figure 15 is the critical temperature  $T_c$  as a function of interaction strength  $|c_0|/(a^3t)$  at the quarter-filling ( $n = 1/2$ ) in  $N_s = 6^3$ .  $T_c$  is obtained through the inflexion point of the curve of pair correlation function  $C_\Delta$ . The parameters used in the calculations are  $\Delta\beta = 0.125/t$ ,  $N_{\text{pretherm}} = 200$ ,  $N_{\text{therm}} = 50$ ,  $N_{\text{sample}} = 1000\text{-}2000$ . Our  $T_c(|c_0|/(a^3t))$  over the interaction strength ranging between BCS and BEC limits is in good agreement with Refs. [47, 48] of the same setup within around 5% of errors, which is within the DQMC results in other literature, ranging around 10% at half-filling ( $n = 1$ ) as shown in the left panel of Fig. 5.13 in Ref. [48].

*b. Dependence of thermal observables on  $\Delta\beta$*

Now that our DQMC calculations with finite  $\Delta\beta$  are confirmed within around 5% of the differences, we have to consider the systematic error from the discretization of temporal direction  $\Delta\beta$ . Figure 21 shows the dependence of various thermal observables on  $\Delta\beta$  by fixing  $T/t = 1/(N_t\Delta\beta t) = 0.4$ . The expectation values of thermal observables are obtained by 1000-2000 samples with  $N_{\text{pretherm}} = 200$  and  $N_{\text{therm}} = 100$  at the one-eighth filling ( $n = 1/4$ ). In Fig. 21, we take the ratio of thermal observables at  $\Delta\beta = 0.125/t$  to those at the continuum limit of the temporal direction  $\Delta\beta \rightarrow 0$  to make the deviations easily visible. As summarized in Table VII, the differences of the observables with  $\Delta\tau = 0.125/t$  and  $\Delta\beta \rightarrow 0$  are around 5% (for  $\chi_P$ ), 10% (for  $C_\Delta$  and  $E/A$ ), and 20% (for  $\mu$ ). Note that we use only  $C_\Delta$  and  $\chi_P$  for obtaining  $T_c$  and  $T^*$  in this work.

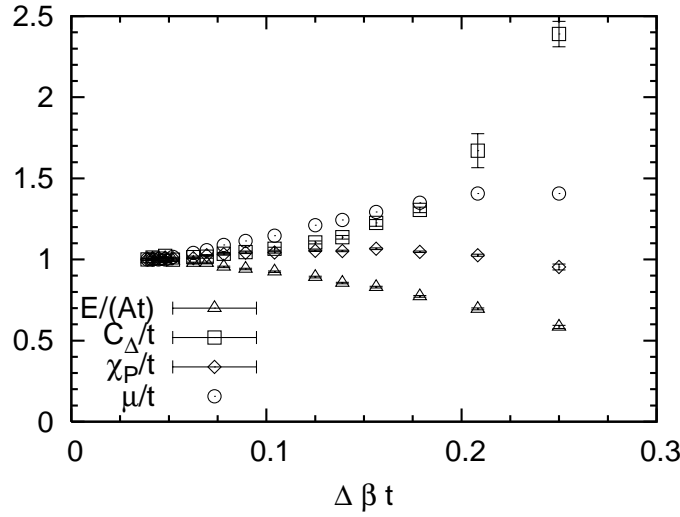


FIG. 21:  $\Delta\beta$  dependence of the ratio of energy per particle  $E/A$ , pair correlation function  $C_\Delta$ , Pauli spin susceptibility  $\chi_P$ , and chemical potential  $\mu$  to those at  $\Delta\beta \rightarrow 0$  at  $T/t = 0.4$  with the interaction strength  $c_0/(a^3t) = -6.0$  at the one-eighth filling ( $n = 1/4$ ) in the dimensionless unit.

Next we examine the influence of finite  $\Delta\beta$  on  $T_c$  and  $T^*$ . Figures 22 and 23 summarize the effect of the finite  $\Delta\beta$  on  $T_c$  and  $T^*$ . As seen in those figures,  $T_c/t = 0.45(1)$  MeV and  $T^*/t = 0.87(2)$  MeV for  $\Delta\beta = 0.125/t$ , and  $T_c/t = 0.47(2)$  MeV and  $T^*/t = 0.79(2)$  MeV for  $\Delta\beta = 0.0625/t$ . The quantities in the parentheses indicate the statistical uncertainties. The deviations in  $T_c$  and  $T^*$  without the statistical errors are around 5% and 10%, respectively.

TABLE VII: Ratio of thermal observables.

$\mathcal{O}$	$\mathcal{O}(\Delta\beta = 0.125/t)$	$\mathcal{O}(\Delta\beta \rightarrow 0)$	$\mathcal{O}(\Delta\beta = 0.125/t)/\mathcal{O}(\Delta\beta \rightarrow 0)$
$E/(At)$	1.449(8)	1.625(8)	0.892(9)
$C_\Delta$	1.45(1)	1.32(1)	1.10(2)
$\chi_P$	0.207(9)	0.1965(9)	1.05(5)
$\mu/t$	1.49(1)	1.23(1)	1.21(1)

We have to count on these discrepancies of around 10% as the systematic error of our final results besides the statistical error.

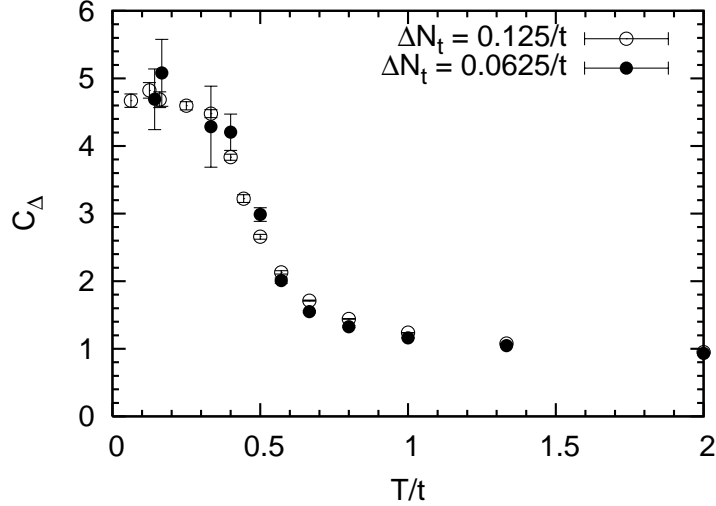


FIG. 22: Pair correlation function  $C_\Delta$  as a function of temperature  $T$  in the unit of hopping amplitude  $t$  at different  $\Delta\beta$  at  $k_F = 30$  MeV,  $N_s = 4^3$ , and  $n = 1/4$ . The open and solid circles with statistical errors are the results at LO and NLO, respectively.

As described in Sec. III, we use  $P_s$  for an estimation of  $\Delta$ . The constant tails of  $P_s$  at the large separation of pairs are  $P_s(\Delta\beta = 0.125/t) = 0.02784(46)$  and  $P_s(\Delta\beta = 0.0625/t) = 0.0295(24)$  at  $k_F = 30$  MeV. The resultant pairing gaps extracted from  $P_s$  through  $\Delta = c_0\sqrt{P_s}$  with  $c_0 = 0.8012$  MeV are  $\Delta(\Delta\beta = 0.125/t) = 0.1337(11)$  MeV and  $\Delta(\Delta\beta = 0.0625/t) = 0.1377(56)$  MeV. The deviation between them without the statistical errors

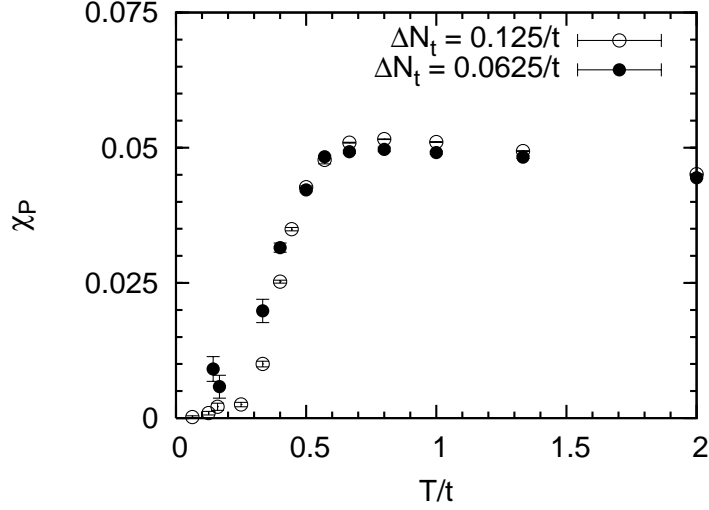


FIG. 23: Pauli spin susceptibility  $\chi_P$  as a function of temperature  $T$  in the unit of hopping amplitude  $t$  at different  $\Delta\beta$  at  $k_F = 30$  MeV,  $N_s = 4^3$ , and  $n = 1/4$ . The open and solid circles with statistical errors are the results at LO and NLO, respectively.

quoted by the parentheses is 0.004 MeV, which results in around 3% of the systematic error.

- 
- [1] D. J. Dean and M. Hjorth-Jensen, Rev. Mod. Phys. **75**, 607 (2003).
  - [2] H. Heiselberg and V. Pandharipande, Ann. Rev. Nucl. Part. Sci. **50**, 481 (2000).
  - [3] U. Lombardo and H. J. Schulze, Lect. Notes Phys. **578**, 30 (2001).
  - [4] G. F. Bertsch and H. Esbensen, Annu. Phys. **209**, 327 (1991); H. Esbensen and G. F. Bertsch, Nucl. Phys. **A542**, 310 (1992).
  - [5] M. Matsuo, K. Mizuyama, and Y. Serizawa, Phys. Rev. C **71**, 064326 (2005); M. Matsuo, Phys. Rev. C **73**, 044309 (2006).
  - [6] K. Hagino and H. Sagawa, Phys. Rev. C **72**, 044321 (2005).
  - [7] J.-R. Buchler and S. A. Coon, Astrophys. J. **212**, 807 (1977).
  - [8] R. B. Wiringa, V. Fiks, and A. Fabrocini, Phys. Rev. C **38**, 1010 (1988).
  - [9] A. Akmal, V. R. Pandharipande, and D. G. Ravenhall, Phys. Rev. C **58**, 1804 (1998).
  - [10] Ø. Elgarøy and M. Hjorth-Jensen, Phys. Rev. C **57**, 1174 (1998).
  - [11] K. Hebeler, A. Schwenk, and B. Friman, Phys. Lett. **B648**, 176 (2007).

- [12] S. C. Pieper, R. B. Wiringa, and J. Carlson, Phys. Rev. C **70**, 054325 (2004); S. C. Pieper, K. Varga, and R. B. Wiringa, Phys. Rev. C **66**, 044310 (2002); S. C. Pieper and R. B. Wiringa, Annu. Rev. Nucl. Part. Sci. **51**, 53 (2001); R. B. Wiringa, S. C. Pieper, J. Carlson, and V. R. Pandharipande, Phys. Rev. C **62**, 014001 (2000); J. Carlson and R. Schiavilla, Rev. Mod. Phys. **70**, 743 (1998), and references therein.
- [13] J. Carlson, Nucl. Phys. **A787**, 516c (2007).
- [14] A. Gezerlis and J. Carlson, Phys. Rev. C **77**, 032801 (2008).
- [15] S. Gandolfi, F. Pederiva, S. Fantoni, and K. E. Schmidt, Phys. Rev. C **73**, 044304 (2006); S. Gandolfi, F. Pederiva, S. Fantoni, and K. E. Schmidt, Phys. Rev. Lett. **99**, 022507 (2007); S. Gandolfi and F. Pederiva, Eur. Phys. J. A **35**, 207 (2008).
- [16] A. Fabrocini, S. Fantoni, A. Yu. Illarionov, and K. E. Schmidt, Phys. Rev. Lett. **95**, 192501 (2005).
- [17] S. Gandolfi, A. Yu. Illarionov, S. Fantoni, F. Pederiva, and K. E. Schmidt, Phys. Rev. Lett. **101**, 132501 (2008).
- [18] D. Lee, arXiv:0804.3501.
- [19] E. Y. Loh Jr. and J. E. Gubernatis, in *Electronic Phase Transitions*, edited by W. Hanke and Yu. V. Kopaev (Elsevier, Amsterdam, 1992).
- [20] R. R. dos Santos, Braz. J. Phys. **33**, 36 (2003).
- [21] H. M. Müller, S. E. Koonin, R. Seki, and U. van Kolck, Phys. Rev. C **61**, 044320 (2000).
- [22] R. Seki, U. van Kolck, and M. J. Savage, *Nuclear Physics with Effective Field Theory; Proceedings of the Joint Caltech/INT Workshop* (World Scientific, Singapore, 1998).
- [23] P. F. Bedaque, M. J. Savage, R. Seki, and U. van Kolck, *Nuclear Physics with Effective Field Theory II; Proceedings of INT Workshop* (World Scientific, Singapore, 2000).
- [24] D. Lee, B. Borasoy, and T. Schäfer, Phys. Rev. C **70**, 014007 (2004); D. Lee and T. Schäfer, *ibid.* **72**, 024006 (2005); D. Lee and T. Schäfer, *ibid.* **73**, 015201 (2006); **73**, 015202 (2006).
- [25] J.-W. Chen and D. B. Kaplan, Phys. Rev. Lett. **92**, 257002 (2004).
- [26] A. J. Leggett, J. Phys. (Paris) **41**, C7–19 (1980); P. Nozieres and S. Schmitt-Rink, J. Low Temp. Phys. **59**, 195 (1985); Q. Chen, J. Stajic, S. Tan, and K. Levin, Phys. Rep. **412**, 1 (2005); and references therein.
- [27] For example, D. M. Brink and R. A. Broglia, *Nuclear Superfluidity; Pairing in Finite Systems* (Cambridge University, Cambridge, England, 2005).

- [28] M. Randeria, in *Bose-Einstein Condensation*, edited by A. Griffin, D. Snoke, and S. Stringari (Cambridge University, Cambridge, England, 1994) p.355.
- [29] T. Abe and R. Seki, Phys. Rev. C **79**, 054003 (2009)
- [30] S. Weinberg, Phys. Lett. **B251**, 288 (1990); Nucl. Phys. **B363**, 3 (1991).
- [31] D. B. Kaplan, M. J. Savage, and M. B. Wise, Phys. Lett. **B424**, 390 (1998); Nucl. Phys. **B534**, 329 (1998); S. R. Beane, P. F. Bedaque, M. J. Savage, and U. van Kolck, *ibid.* **A700**, 377 (2002); and references therein.
- [32] U. van Kolck, Nucl. Phys. **A645**, 273 (1999)
- [33] G. P. Lepage, Lecture at the VIII Jorge André Swieca Summer School, Brazil, 1997, arXiv:nucl-th/9706029.
- [34] T. Abe, R. Seki, and A. N. Kocharian, Phys. Rev. C **70**, 014315 (2004); **71**, 059902(E) (2005).
- [35] S. R. Beane, T. D. Cohen, and D. R. Phillips, Nucl. Phys. **A632**, 445 (1998).
- [36] R. Machleidt, Phys. Rev. C **63**, 024001 (2001). See Table XIV for a recent compilation.
- [37] R. Seki and U. van Kolck, Phys. Rev. C **73**, 044006 (2006).
- [38] H. J. Rothe, *Lattice Gauge Theories: An Introduction*, World Scientific Lecture Notes in Physics, 3rd ed. (World Scientific, Singapore, 2005); J. Smit, *Introduction to Quantum Fields on a Lattice* (Cambridge University, Cambridge, England, 2002); I. Montvay and G. Münster, *Quantum Fields on a Lattice*, Cambridge Monographs on Mathematical Physics (Cambridge University, Cambridge, England, 1997); M. Creutz, *Quarks, Gluons and Lattices*, Cambridge Monographs on Mathematical Physics (Cambridge University, Cambridge, England, 1985); and references quoted therein.
- [39] G. H. Lang, G. W. Johnson, S. E. Koonin, and W. E. Ormand, Phys. Rev. C **48**, 1518 (1993).
- [40] U. van Kolck, Phys. Rev. C **49**, 2932 (1994); P. F. Bedaque, H.-W. Hammer, and U. van Kolck, Nucl. Phys. **A676**, 357 (2000); P. B. Bedaque and U. van Kolck, Annu. Rev. Nucl. Part. Sci. **52**, 339 (2002).
- [41] J. W. Negele and H. Orland, *Quantum Many-Particle Systems* (Addison-Wesley, Redwood City, CA, 1988) Chap. 7 (see Prob. 7.1).
- [42] E. Burovski, N. Prokofév, B. Svistunov, and M. Troyer, Phys. Rev. Lett. **96**, 160402 (2006); New J. Phys. **8**, 153 (2006).
- [43] M. Guerrero, G. Ortiz, and J. E. Gubernatis, Phys. Rev. B **62**, 600 (2000).



- [44] A. Moreo and D. J. Scalapino, Phys. Rev. Lett. **66**, 946 (1991).
- [45] R. R. dos Santos, Phys. Rev. B **48**, 3976 (1993).
- [46] R. R. dos Santos, Phys. Rev. B **50**, 635 (1994).
- [47] A. Sewer, X. Zotos, and H. Beck, Phys. Rev. B **66**, 140504(R) (2002).
- [48] A. Sewer, Ph.D. thesis, Université de Neuchâtel, 2002.
- [49] T. Schneider and J. M. Singer, *Phase Transition Approach to High Temperature Superconductivity* (Imperial College Press, London, 2000).
- [50] N. Goldenfeld, *Lectures on Phase Transitions and the Renormalization Group* (Addison-Wesley, Reading, MA, 1992); J. G. Brankov, D. M. Danchev, and N. S. Tonchev, *Theory of Critical Phenomena in Finite-Size Systems; Scaling and Quantum Effects* (World Scientific, Singapore, 2000).
- [51] J. R. Engelbrecht and H. Zhao, arXiv:cond-mat/0110356.
- [52] G. Ódor, Rev. Mod. Phys. **76**, 663 (2004); A. Pelissetto and E. Vicari, Phys. Rep. **368**, 549 (2002).
- [53] I. F. Herbut and Z. Tešanović, Phys. Rev. Lett. **76**, 4588 (1996); and references therein.
- [54] Ø. Elgarøy, L. Engvik, M. Hjorth-Jensen, and E. Osnes, Nucl. Phys. **A604**, 466 (1996).
- [55] J. Wambach, T. L. Ainsworth, and D. Pines, Nucl. Phys. **A555**, 128 (1993).
- [56] For example, J. R. Schrieffer, *Theory of Superconductivity* (Benjamin, New York, 1964), p.55.
- [57] R. B. Wiringa, V. G. J. Stoks, and R. Schiavilla, Phys. Rev. C **51**, 38 (1995).
- [58] V. G. J. Stoks, R. A. M. Klomp, C. P. F. Terheggen, and J. J. de Swart, Phys. Rev. C **49**, 2950 (1994).
- [59] R. Machleidt, F. Sammarruca, and Y. Song, Phys. Rev. C **53**, R1483 (1996).
- [60] H. J. Schulze, J. Cugnon, A. Lejeune, M. Baldo, and U. Lombardo, Phys. Lett. **B375**, 1 (1996).
- [61] L. G. Cao, U. Lombardo, and P. Schuck, Phys. Rev. C **74**, 064301 (2006).
- [62] J. M. C. Chen, J. W. Clark, R. D. Davé, and V. V. Khodel, Nucl. Phys. **A555**, 59 (1993).
- [63] A. Schwenk, B. Friman, and G. E. Brown, Nucl. Phys. **A713**, 191 (2003).
- [64] J. Margueron, H. Sagawa, and K. Hagino, Phys. Rev. C **77**, 054309 (2008).
- [65] R. T. Scalettar, D. J. Scalapino, R. L. Sugar, and D. Toussaint, Phys. Rev. B **36**, 8632 (1987).
- [66] D. R. Phillips, S. R. Beane, and T. D. Cohen, Ann. Phys. (N.Y.) **263**, 255 (1998).

- [67] H. P. Noyes, *Annu. Rev. Nucl. Sci.* **22**, 465 (1972).
- [68] G. Breit, K. A. Friedman, J. M. Holt, and R. E. Seamon, *Phys. Rev.* **170**, 1424 (1968).
- [69] M. C. Birse, J. A. McGovern, and K. G. Richardson, *Phys. Lett.* **B464**, 169 (1999).
- [70] S. E. Koonin and D. C. Meredith, *Computational Physics* (Addison-Wesley, Reading, MA, 1990).